Editors' Suggestion

Experimental investigations of liquid falling films flowing under an inclined planar substrate

Alexandros Charogiannis,[1] Fabian Denner,[2,3] Berend G. M. van Wachem,[3] Serafim Kalliadasis,[4] Benoit Scheid,[5] and Christos N. Markides[1,*]

[1]*Clean Energy Processes (CEP) Laboratory, Department of Chemical Engineering, Imperial College London, London SW7 2AZ, United Kingdom*

[2]*Department of Mechanical Engineering, Imperial College London, London SW7 2AZ, United Kingdom*

[3]*Chair of Mechanical Process Engineering, Otto-von-Guericke-Universitt Magdeburg Universittsplatz 2, 39106 Magdeburg, Germany*

[4]*Department of Chemical Engineering, Imperial College London, London SW7 2AZ, United Kingdom*

[5]*TIPs, Université Libre de Bruxelles, Avenue F.D. Roosevelt 50 1050 Bruxelles, Belgium*

(Received 26 February 2018; published 9 November 2018)

We report on detailed and systematic experiments of thin liquid films flowing as a result of the action of gravity under an inverted planar substrate. A measurement technique based on planar laser-induced fluorescence (PLIF) was developed and applied to a range of such flows in order to provide detailed space- and time-resolved film-height information. Specifically, the experimental campaign spanned three inclination angles ($\beta = -15^\circ$, -30°, and -45°, in all cases negative with respect to the vertical), two water-glycerol solutions (with Kapitza numbers of Ka = 13.1 and 330), and flow Reynolds numbers covering the range Re = 0.6–193. The collection optics were arranged so as to interrogate a spanwise section of the flow extending about 40 mm symmetrically on either side the centerline of the film span (80 mm in total), at a distance 330 mm downstream of the flow inlet. A range of flow regimes, typically characterized by strong three dimensionality and pronounced rivulet formation, were observed depending on the imposed inlet flow conditions. In the lower liquid Kapitza number Ka (=13.1) flows and depending on the flow Re, the free surface of the film was populated by smooth rivulets or regular sequences of solitary pulses that traveled over the rivulets. In the higher liquid Ka (=330) flows, rivulets were observed typically above Re $\approx$ 30, depending also on the inclination angle, and grew in amplitude until quasi-two-dimensional fronts developed intermittently that were associated with distinct thin-film regions of varying length and frequency. These regions are of particular interest as they are expected to affect strongly the heat and mass transfer capabilities of these flows. The occurrence of the fronts was more pronounced, with higher wave frequencies, in film flows at smaller negative inclinations for the same flow Re. The rivulet amplitude was found to increase at larger inclinations for the same Re and showed a nonmonotonic trend with increasing Re, reaching a maximum that shifted to higher Re at larger inclinations. Furthermore, in flows that displayed pronounced rivulet formation [i.e., large (negative) β and higher Re], the local film-height standard deviation in regions corresponding to the rivulet crests and troughs was reduced compared to the film-height standard deviation calculated over the entire examined film region. The mean rivulet wavelength also increased at larger inclinations, peaking at 26 mm when Ka = 330. Based on our experimental results and theoretical arguments, we hypothesize that the formation of rivulets can be attributed, at small β, to a secondary Rayleigh-Taylor instability mechanism that destabilizes the suspended two-dimensional wavefronts, and at

*Corresponding author: c.markides@imperial.ac.uk

larger β, to the primary Rayleigh-Taylor instability mechanism of a flat film coating the underside of the inclined plate.

DOI: 10.1103/PhysRevFluids.3.114002

I. INTRODUCTION

"Falling" liquid films, flowing under the action of gravity, exhibit a range of intriguing flow phenomena that have motivated numerous studies since the pioneering work of Kapitza and Kapitza [1,2]. Falling films can be viewed as simple prototypes of open-flow hydrodynamic and nonlinear systems in general, and therefore their study has attracted considerable fundamental and theoretical interest; beyond this, however, such flows play a central role in the development of high-performance, effective, and compact heat- and mass-transfer components in a wide variety of practical applications. These include, among others, wetted-wall absorbers, heat exchangers, film condensers, evaporators or reactors, and microcooling schemes. Commonly studied flows include gravity-driven liquid films falling over inclined plates [3–6], gaseous shear-driven liquid films over horizontal plates [7], and liquid films falling down the inner or outer surfaces of tubes or pipes (annular or annulus flows) with or without a co- or countercurrent gas-shear flow in the core of the cross section [8–10].

Despite the considerable attention these flow configurations and numerous variations thereof have received, only a few studies have been dedicated to liquid films falling down the *underside* of inclined substrates, that is, with gravity destabilizing the flow. The present experimental effort is therefore motivated by the limited qualitative and quantitative information that is available on the flow characteristics and phenomenology of these flows and by a desire to generate detailed spatiotemporal data that is currently unavailable, as a means for better understanding the complex underlying flow phenomena. Depending on the liquid flow rate, substrate inclination angle, and liquid properties, we observe a range of flow regimes typically characterized by strong three dimensionality, film contraction in the cross-stream direction of the flow, and pronounced film-height modulation in the transverse direction of the flow (i.e., rivulet formation). For reference and also to facilitate the upcoming literature review, in Fig. 1, we showcase some of these regimes using space- and time-resolved film-height maps recovered by application of planar laser-induced fluorescence imaging (PLIF).

Following a brief introduction to the aforementioned flow phenomena, we proceed to discuss notable research efforts dedicated to the study of inverted falling films and pendant rivulets. We then provide a description of our experimental apparatus and the optical technique that was developed to allow spatiotemporally resolved film-height measurements in the flows of interest, followed by a presentation and discussion of our experimental results. Our experimental campaign comprises two aqueous-glycerol solutions (and hence two different Kapitza number, Ka, liquids) and three substrate inclination angles, $\beta = -15^\circ$, -30°, and -45°, and spans Reynolds numbers in the range $\mathrm{Re} = 0.6$–193. We emphasize that only conditions with no dripping and no film rupture were investigated and that all measurements were performed in planar films rather than individual rivulets; the latter being the case with most experimental investigations found in the literature. With the present study, we build upon our previous one on the interfacial topology of inverted falling-films, which only spanned low-Re ($\mathrm{Re} = 0.6$–8.2) films falling down a $\beta = -30^\circ$ incline (see Ref. [11]), and at the same time seek to provide an extensive experimental dataset that could encourage further experimental investigations and provide a solid foundation for novel numerical investigations. In addition to the wider Re, β, and Ka ranges that we introduce, the data-processing methodologies that we developed and presented in Ref. [11], relating primarily to the spatiotemporal frequency content of the interfacial fluctuations in these flows, are hereby complemented by a comprehensive analysis of film-height statistics. A concise presentation of the experimental apparatus and optical techniques that we developed for the purposes of this study,

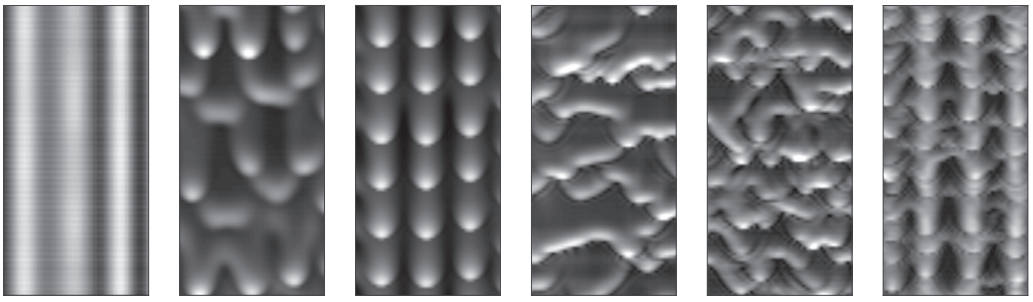

FIG. 1. Wave patterns obtained by application of PLIF, with the light sheet arranged along the transverse direction of the flow. The flow Reynolds number, Re, fluid Kapitza number, Ka, and inclination angle, β, take the following values: (a) Re $= 0.6$, Ka $= 13.1$, and $\beta = -30^\circ$, (b) Re $= 3.5$, Ka $= 13.1$, and $\beta = -30^\circ$, (c) Re $= 7.4$, Ka $= 13.1$, and $\beta = -30^\circ$, (d) Re $= 19$, Ka $= 330$, and $\beta = -15^\circ$, (e) Re $= 36$, Ka $= 330$, and $\beta = -30^\circ$, and (f) Re $= 118$, Ka $= 330$, and $\beta = -45^\circ$.

and which are shared with the experimental investigation in Ref. [11], have been included for completeness but also to facilitate our discussion of the topological features of the investigated flows.

A. Three-dimensional waves in falling-film flows

A thin liquid-film falling down an inclined plane is unstable to long-wave perturbations above a critical Reynolds number, $\mathrm{Re_c}$, instigating the formation of hydrodynamic waves on its free surface [12]. The instability mechanism is founded upon the phase shift between the interface displacement and vorticity, which is caused by inertia (described in detail in Refs. [13–16]). Surface tension, viscosity, and the cross-stream component of gravity stabilize the flow, while inertia and the streamwise component of gravity destabilize it. Naturally developing free-surface instabilities emerge past a short-lived flat-film region, evolve into two-dimensional (2-D) solitary-wave trains, and which sufficiently far from the inlet break down into complex wave patterns comprising localized three-dimensional (3-D) pulses that interact continuously with each other [16–24].

In recent years, numerous researchers have been investigating these transitions in order to obtain a comprehensive description of the 3-D waves [25–27] that develop on falling liquid-film flows. Alekseenko *et al.* [28] and Demekhin *et al.* [29–32], for example, studied the spatiotemporal evolution of and generation of horseshoe-shaped 3-D solitary pulses, also referred to as Λ solitons, in vertically falling water films, and reported that above Re ≈ 40, 2-D solitary waves become unstable to transverse perturbations and eventually disintegrate, giving rise to surface turbulence. Yoshimura *et al.* [33] and later Park and Nosoko [34] conducted shadowgraphy experiments in water films (Ka ≈ 3000) falling down a vertical plate and reported 3-D horseshoe-shaped fronts preceded by capillary ripples above Re ≈ 40 in liquid films with Ka ≈ 1000. The capillary ripples of adjacent pulses were shown to interact and generate clusters of dimples, which eventually disintegrated and dissipated. Adomeit and Renz [35] observed U- and W-shaped waves at Re $= 27$, elongated streaklike waves and larger wave structures referred to as surgelike waves at Re $= 72$, and primarily turbulent surgelike waves at Re $= 196$.

More recently, Alekseenko and coworkers [36–38] reported the formation of rivulets on isothermal films (vertically falling water and water-glycerol films). This formation is manifested by a "quasisinusoidal" modulation of the interface height in the transverse direction of the flow [39–42], and has been attributed, when observed in nonisothermal falling films, to surface-tension variations induced by temperature gradients (and described by the long-wave thermocapillary Marangoni instability mechanism). Joo *et al.* [43] proposed a mechanism for the formation of rivulets on

the surface of a thin liquid layer falling down a heated substrate at low Re (Re $\approx$ 1), while Scheid and coworkers [44,45] introduced a theoretical framework for the investigation of the Marangoni-driven rivulet formation in an effort to identify possible heat-transfer enhancements in the presence of rivulets. By varying the flow Re in the range Re = 0.5–10 in water films flowing down a uniformly heated vertical wall, these authors captured numerically Marangoni-driven waves in the region where the transition from the drag-gravity to the drag-inertia regimes for isothermal flows occurs. Interestingly, some of the wave patterns that were presented in these studies resemble closely the ones we observed in our experiments with Ka = 13.1 and $\beta = -30^\circ$ [see, for example, Figs. 1(a)–1(c)].

In the experiments of Alekseenko and coworkers [36–38], at higher Re and under isothermal flow conditions, the topology of liquid films falling down a vertical plate was examined by employing LIF, which allowed space- and time-resolved film-height measurements over an extended 2-D domain. Two scenarios of rivulet formation and evolution were discussed: (i) Above Re $\approx$ 30 for water and Re $\approx$ 12 for water-glycerol films, forward horseshoe-shaped protrusions appeared at the crests of 2-D solitary waves a few wavelengths downstream of the flow inlet, while lower curvature waves, referred to as "walls" by the authors, formed between the protrusions. The wakes of these protrusions perturbed the crests of the trailing waves and triggered the generation of rivulets. The rivulet amplitude was shown to increase monotonically with increasing distance from the flow inlet. (ii) When the film was perturbed by a regular grid of needles that was placed at the flow inlet, a time-averaged redistribution of liquid was observed at all examined Re. In addition, over the range Re $\approx$ 10–60, film forcing was shown to move the rivulet inception zone further upstream compared to the unperturbed cases, allowing time for neighboring rivulets to gradually merge far downstream and thus to increase in amplitude and wavelength. The formation of rivulets was linked, in both cases, to liquid drainage from the residual layer between decaying 2-D solitary pulses and into the forward protrusions of the trailing waves. Furthermore, a "capillary-precursor-induced" mechanism was proposed, according to which the liquid flow along the strongly bent capillary ridges and troughs of the precursor film resulted in an influx of liquid into the horseshoe-shaped protrusions.

B. Liquid films flowing down inverted substrates

Rothrock [46] pioneered the experimental study of liquid films falling down an inverted planar substrate and complemented his experimental measurements with a linear-stability analysis. He obtained the onset conditions for wave formation on a pendant rivulet and demonstrated the development of solitary waves which either travel down the rivulet or grow into much larger structures and eventually fall off. In addition, he observed that a film flowing down an inverted substrate destabilizes rapidly and forms rivulets due to the combined effects of surface tension (which stabilizes the flow) and the cross-stream component of gravity (which destabilizes the flow). The combination of these two forces is also responsible for pulling the outer edges of the film toward the center, in a similar fashion to the phenomenon of film contraction (or film shrinkage) in the case of a liquid film flowing over a heated substrate [47–49]. Eventually, the wedge-shaped film converges into a single rivulet with constant width.

Liquid drop falloff from viscous (water-glycerol) pendant rivulets was later studied by Indeikina *et al.* [50], who derived conditions for drop falloff using a long-wave lubrication equation as a function of the capillary length, rivulet width, static contact angle, and inclination angle. Two falloff mechanisms were identified, one linked to failure of the mean-flow enhanced axial curvature to counteract gravity and limit fluid drainage into the drop, and one attributed to failure of the azimuthal curvature, as in the Rayleigh-Plateau (R-T) instability mechanism. Different drop formation and falloff scenarios were observed depending on the rivulet mean flow rate; at higher flow rates, falloff occurred in the form of a liquid jet that detached from the substrate, while at intermediate flow rates, large rounded drops detached from the rivulet surface. At low flow rates, small amplitude

waves formed near the inlet and coalesced into larger droplike structures which, however, did not detach.

Alekseenko *et al.* [51] performed experiments concerned with rivulet and hydrodynamic-wave formation in ethanol flows on the underside of a cylinder inclined between 2° and 15° to the horizontal, over the range Re = 3.6–57. By measuring the rivulet thickness along the axial direction of the flow, similar wave profiles were recovered to those observed in conventional falling films on planar substrates, while liquid ejection from the substrate was shown to occur above a critical flow rate in accordance with the falloff mechanisms proposed by Indeikina *et al.* [50]. The same flows were later examined by application of particle image velocity (PIV) [52], which revealed that the flow field underneath the main wave humps was dominated by a vortex (in a reference frame moving with the wave speed) and that velocity profiles along the axial direction of the flow were "fuller" at the wave crests and fronts than self-similar parabolic profiles, and increasingly so for larger wave amplitudes.

Unlike the usual liquid films flowing over planar inclined surfaces, which only exhibit convectively unstable behavior, liquid films flowing down the underside of inclined surfaces can exhibit absolutely unstable behavior. In the limiting case of a film suspended under a horizontal substrate, the film-free surface deforms in accordance with the R-T instability mechanism, with gravity destabilizing the flow and surface tension restoring it. Brun *et al.* [53] investigated the development of both absolute and convective instabilities in flows underlying moderately tilted substrates, and noted that interface deformations move downstream when the substrate inclination is reduced and that dripping ceases above a critical inclination angle. This behavior was attributed to the transition from the absolute- to the convective-instability regime. Scheid *et al.* [54] extended this study to larger Re (above the limit of negligible inertia) and reported that the critical angle for the transition is specific to both the fluid and the flow rate. Moreover, they showed that the latter does not vary monotonically with the flow Re and instead exhibits a minimum value; this value, in turn, approaches the limiting case of a film suspended underneath a horizontal substrate with increasing Ka number. Recently, Kofman *et al.* [55] showed that the dripping transition is governed by nonlinearities and does not coincide with the absolute/convective transition as the Re is increased, even though both transitions share qualitative features such as a minimum critical angle. Rohlfs *et al.* [56] investigated the topology and velocity field underneath the 2-D waves forming on the free surface of films falling underneath a planar substrate, by conducting direct numerical simulations (DNSs). These authors demonstrated the presence of eddies in the main wave humps and rotating vortices in the capillary-wave troughs, and extended the correlations they derived for the onset of flow recirculation and flow reversal under stabilizing gravity to inverted flows [57].

In contrast to the aforementioned studies, Lin *et al.* [58] employed a model based on the lubrication approximation with negligible inertia and assuming a nonwetted substrate that allowed for the presence of contact lines (fronts). Based on this model, these investigators suggested that the topology of the observed waves is governed by a single parameter which includes the capillary number, Ca, and the inclination angle. Based on 3-D simulations, the same authors later reported that the fronts broke down into fingerlike structures as the inclination approached the limiting, horizontal case and that droplike waves rode these fingers and raced downstream with speeds exceeding the propagation speeds of the fronts [59]. It should be noted that the formation of fingers distributed perpendicularly to the main flow direction has been investigated extensively in liquid films spreading over planar substrates, both theoretically as well as experimentally [60–63].

Finally, Rietz *et al.* [64] examined the evolution of the surface topology of viscous (Ka = 5.1) films flowing down the outer surface of a vertical rotating cylinder using high-speed visualization, as a function of the liquid flow rate (and hence the flow Re, which was increased up to Re = 1.6) and the rotational speed. Increasing the latter results in an increase in the centrifugal force, which destabilizes the film in a manner equivalent to the cross-stream component of gravity in the case of a liquid film falling down an inverted substrate. Both the rivulet wavelengths and inception lengths were shown to agree well with predictions based on the R-T instability mechanism. Moreover, the rivulet inception length was shown to decrease when the destabilizing force was increased,

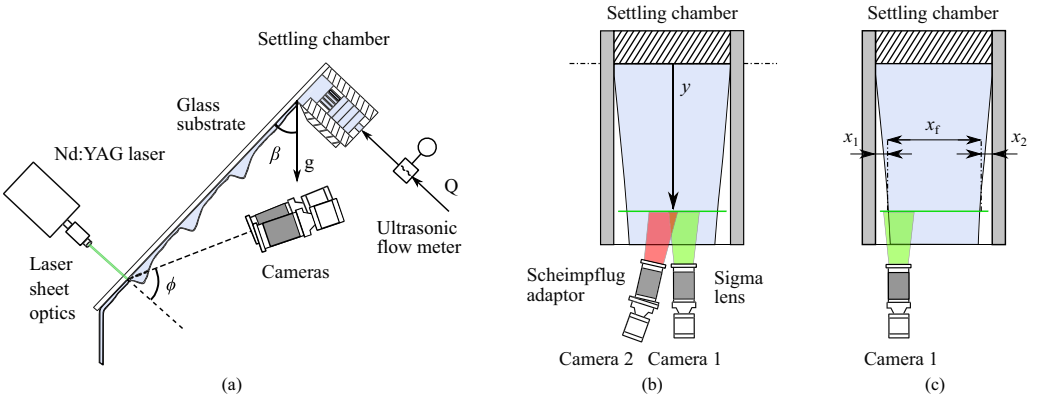

FIG. 2. Schematic of our experimental arrangement showing the orientation of the laser sheet and cameras. [(a), (b)] Two-camera setup relative to the test section from the side and from above. (c) Single-camera setup from above. Angle β corresponds to the substrate inclination angle relative to the vertical, and angle ϕ to the angle formed between the excitation plane normal and the view of the cameras.

which, along with evidence from numerical simulations, suggests that rivulets always develop given a nonzero destabilizing force and sufficient evolution length.

Our short review of selected studies concerned with the development of complex wave phenomena on the free surface of liquid films flowing over inclined planar substrates (see Sec. I A) is by no means exhaustive, yet it portrays the wealth of information that has been obtained from such efforts. In contrast, as we show in Sec. I B, research studies relating to liquid films flowing *under* inclined planar substrates are rather scarce and mainly focus on the identification of onset conditions for liquid ejection from individual pendant rivulets, the description of the physical mechanisms underlying the different liquid-detachment phenomena (i.e., liquid jets and large rounded drops), and the transition from the absolute- to the convective-instability regime as a function of liquid flow rate and the fluid properties. The limited availability of experimental data relating to liquid films falling down inverted substrates highlights the need for further research on this particular class of interfacial flows, and this is the main motivation for the present study.

II. EXPERIMENTAL APPARATUS

A. Flow facility

The flow facility was employed previously for the investigation of the hydrodynamic characteristics of isothermal falling films [3–6] and the thermal and hydrodynamic characteristics of heated falling films [42,65] and was suitably modified here for the purposes of this study. Specifically, the test section was inverted and the collection and laser-sheet optics were placed underneath it [see Fig. 2(a)]. In the experiments, liquid was pumped via a counterflow heat exchanger, which maintained a constant flow temperature, into the settling chamber, which dispensed the flow evenly across the test section. The liquid flow rate was controlled by varying the power input to the pump and measured by an ultrasonic flow meter.

The two primary dimensionless numbers that characterize the film flows, the flow Reynolds number, Re, and the liquid Kapitza number, Ka, are defined below. The former is defined based on the mean flow rate, Q, per unit span, x_f, of the flow *at the measurement location*, $\Gamma = Q/x_f$, and the fluid kinematic viscosity, ν_f, such that

$$\mathrm{Re} = \frac{\Gamma}{\nu_f}, \tag{1}$$

while the latter is defined using the fluid surface tension, σ_f, density, ρ_f, kinematic viscosity, ν_f, and the gravitational constant, g, according to

$$\mathrm{Ka} = \frac{\sigma_f}{\rho_f \nu_f^{4/3} g^{1/3}} . \tag{2}$$

It should be noted that in the above definition of Ka, the inclination angle dependence has been excluded such that Ka depends on the fluid properties alone, rather convenient from the experimental point of view.

Our test section comprises a $0.7 \times 400 \times 290$-mm soda-lime glass plate, mounted on an aluminium frame. Hinges installed on either side of the frame allow for the inclination angle to be varied; in these experiments β was set to $-15°$, $-30°$, and $-45°$. When preparing for a measurement run, the liquid flow rate was first set to the maximum value intended for the experiment, and the entire test section was wetted. Through the combined action of gravity and surface tension, the film then contracted as contact lines formed far downstream on either side of the test section and gradually moved upstream and closer to the flow inlet [Figs. 2(b) and 2(c)]. The film span at the downstream location where imaging experiments were performed, x_f, was recorded for each experimental run and is provided in Table III. The obtained x_f values were reproducible during trial experiments in which the flow was halted and then reintroduced over the plate, to within 10–20 mm. All measurement runs were conducted by gradually reducing the flow rate, and thus the flow Re, down to the lowest setting, which prevented the film from contracting any further. Instead, the film was narrower when a low flow rate was established first and then expanded with increasing flow rate. We opted for the first approach as it allowed us to adjust the flow Re by modulating the flow rate alone, rather than letting it vary with both the flow rate and the film span, which would impair our ability to compare directly any film-height statistics obtained from flows with different film spans.

B. Optical arrangement

The optical arrangement comprises a double-cavity Nd:YAG laser (Litron Lasers, Nano-L-50-100PV) and two 10-bit CMOS cameras (LaVision, VC-Imager Pro HS 500), which were operated at a rate of 200 Hz and were synchronized using a LaVision High-Speed Controller (HSC). The liquid flow was seeded with a fluorescent dye (Rhodamine-B) at a concentration of approximately 10 mg/L and was excited by a thin ($\approx$200 μm) laser sheet which extended along the span of the glass plate. Both cameras were equipped with Sigma 105-mm $f/2.8$ macro lenses and extension rings in order to achieve the desired magnification and long-pass optical filters (cutoff wavelength of 540 nm) in order to prevent the collection of scattered laser light.

The orientation of the laser sheet and cameras relative to the test section, when viewed from the side, is presented in Fig. 2(a), while a schematic of the test section showing the location of the excitation plane relative to the flow inlet and the spanwise orientation of the two cameras relative to the excitation plane, is provided in Fig. 2(b). The field of view of the two-camera setup extends symmetrically about the middle of the test section in the spanwise direction of the flow. The second arrangement shown in Fig. 2(c) employs a single camera and was used to visualize a flow region that extended inward from the film-contact line in a separate set of experiments. The angle ϕ between the excitation plane and the cameras [Fig. 2(a)] corresponds to $\approx$55°; the maximum value that could be achieved without direct contact between the cameras and the settling chamber.

The dye-doped liquid was excited from the solid-liquid interface side, and the emitted fluorescence was collected from the gas-liquid interface side. Prior to conducting imaging experiments, the imaging planes of the cameras were mapped and corrected for perspective distortions using a Perspex plate with a calibration target attached to it. The plate was carefully aligned with the excitation plane and held against gravity using magnets. The fields of view of the two cameras overlapped by $\approx$15 mm, which allowed an expanded measurement domain by "stitching" of the obtained film-height measurements from each camera. The final measurement domain corresponds to $\approx$80–85 mm for the two-camera setup, and to $\approx$48 mm for the single-camera setup depending on the measure-

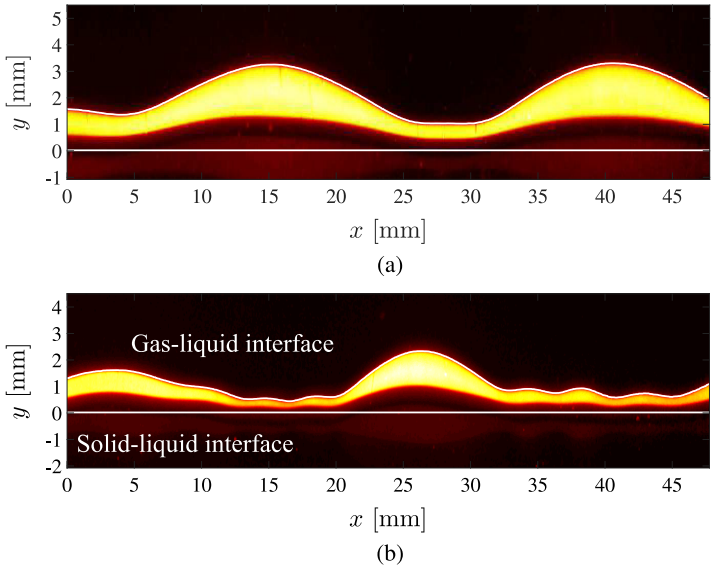

FIG. 3. PLIF images after correction for perspective distortion, taken from flows with (a) Re = 8.2, Ka = 13.1, and $\beta = -30^\circ$ (reproduced from Fig. 2 in Ref. [11]) and (b) Re = 155, Ka = 330, and $\beta = -45^\circ$.

ment run. The spatial resolution of the imaging arrangement corresponds to $\approx$38 μm/pixel, and all film-height measurements were collected at a distance $y = 330$ mm downstream of the flow inlet.

III. EXPERIMENTAL METHODOLOGY

A. Data acquisition and processing

PLIF images were recorded at a rate of 200 Hz and over a period of 10 s for each examined film-flow condition (i.e., for each Ka, Re, and β combination). Sample PLIF images, which were first corrected for perspective distortions, are presented in Fig. 3 for flows with Ka = 13.1, Re = 8.2, and $\beta = -30^\circ$ and Ka = 330, Re = 155, and $\beta = -45^\circ$.

Referring to either image, it is evident that the solid-liquid interface cannot be located directly based on the emitted fluorescence, which tracks the waviness of the gas-liquid interface. In addition, owing to the refractive index change (from the liquid to the surrounding air), the fluorescence emission appears "squashed" along the cross-stream direction of the flow (y axis in Fig. 3). Thus, an alternative methodology was developed. A solution comprising ethanol and Rhodamine-B was prepared and applied on the glass, at the region that would normally be illuminated by the laser sheet. Ethanol was preferred to water due to its favorable wetting properties and higher volatility. Once the ethanol evaporated, the glass remained stained and the fluorescence emitted by the residual Rhodamine layer was used as a marker for the solid-liquid interface.

Close inspection of the intensity profile in Fig. 4(a), extracted from a PLIF image of the Rhodamine-stained substrate, reveals that the signal intensity increases and subsequently decreases over a number of pixels, rather than abruptly over successive pixels. In greater detail, a low-intensity peak is observed near the main, high-intensity peak, the latter originating from the illuminated Rhodamine layer and the former from a reflection of the Rhodamine emission about the glass surface that is not in contact with the flow. Ahead of the high-intensity peak, the signal gradient decreases abruptly at $I \approx 25$. Some of the causes that contribute to this "blurring" of the PLIF intensity profile include the finite thickness and Gaussian profile of the laser sheet, the acute angle formed between the excitation and imaging planes, and the presence of secondary reflections from the two glass surfaces.

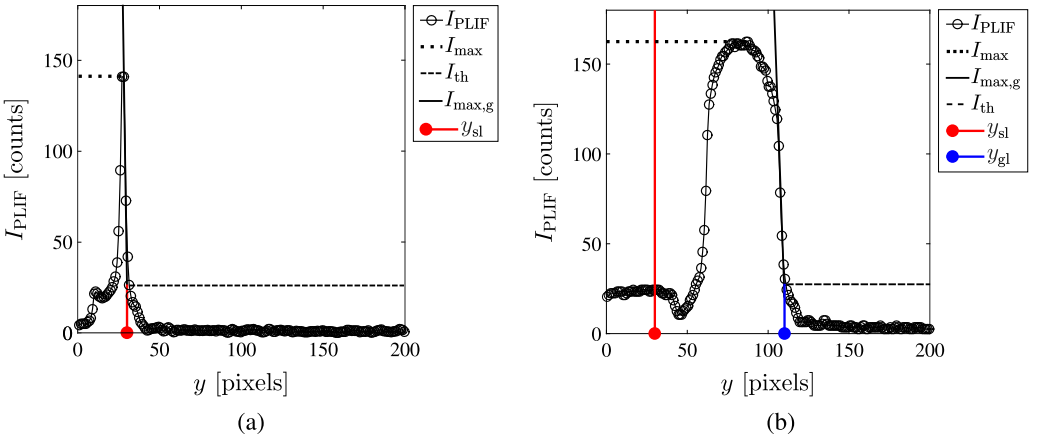

FIG. 4. PLIF intensity profile across the (a) Rhodamine-stained glass substrate and (b) liquid domain, from which the location of the solid-liquid and gas-liquid interfaces were recovered, respectively.

In our experiments, the location of the solid-liquid interface, y_{sl}, was obtained on a per-column basis from the intercept between the maximum-gradient line, $I_{\max,g}$, and a threshold signal level, I_{th}, in a region bounded by the maximum signal intensity, $I_{\max}$, and the threshold intensity,

$$y_{\mathrm{sl}} = \arg_y[I_{\max,g} - I_{\mathrm{th}}(y) = 0];\ I_{\max,g} = \left.\frac{dI}{dy}\right|_{\max}. \tag{3}$$

The latter was determined by tracking the intensity gradient locally and identifying the coordinate where its absolute value fell abruptly. The same approach was used in the PLIF images collected during the film-flow experiments to locate the gas-liquid interface, y_{gl} [see Fig. 4(b)], as we sought to incorporate all of the aforementioned considerations regarding the blurring of the fluorescence emission in order to track accurately the disparity between the two liquid boundaries along the imaging plane. Both gas-liquid and solid-liquid interface identification routines were implemented in MATLAB by means of a processing algorithm that was developed in house.

B. Technique validation

A series of experiments were conducted for error estimation and quality assurance purposes. Towards that end, the test section was inclined at $\beta \approx 20^\circ$ and $\beta \approx 45^\circ$, and the laser-sheet optics were migrated closer to the flow inlet. The angle ϕ formed between the excitation and camera planes [see Fig. 2(a)], as well as the magnification of the collection optics, were reproduced in an effort to replicate the original configuration as closely as possible. Film-height measurements were collected at a distance $y = 50$ mm downstream of the flow inlet; a location that was selected on the basis that the examined film flows are locally relatively flat, and thus an excellent approximation of the mean film height could be obtained from the one-dimensional, steady, fully developed solution of the Navier-Stokes equation for a gravity-driven flow, also referred to as the Nusselt solution [66]. The Nusselt height, h_{N}, is calculated according to

$$h_{\mathrm{N}} = \left(\frac{3\nu Q}{g x_{\mathrm{f}} \sin\beta}\right)^{1/3} = \left(\frac{3\nu^2 \mathrm{Re}}{g \sin\beta}\right)^{1/3}. \tag{4}$$

The flow Re was varied in the range Re = 0.5–80 by varying the liquid flow-rate and kinematic viscosity, the latter by increasing the glycerol content from 49% to 82% glycerol by weight. Based on the imposed flow conditions, the Nusselt height was varied in the range $h_{\mathrm{N}} \approx 0.5$–3 mm. Two measurement sets were generated, one by employment of Eq. (3) for the identification of the solid-liquid and gas-liquid interfaces with $I_{\mathrm{th}}(y) \neq 0$, and one with $I_{\mathrm{th}} = 0$ when locating the gas-liquid

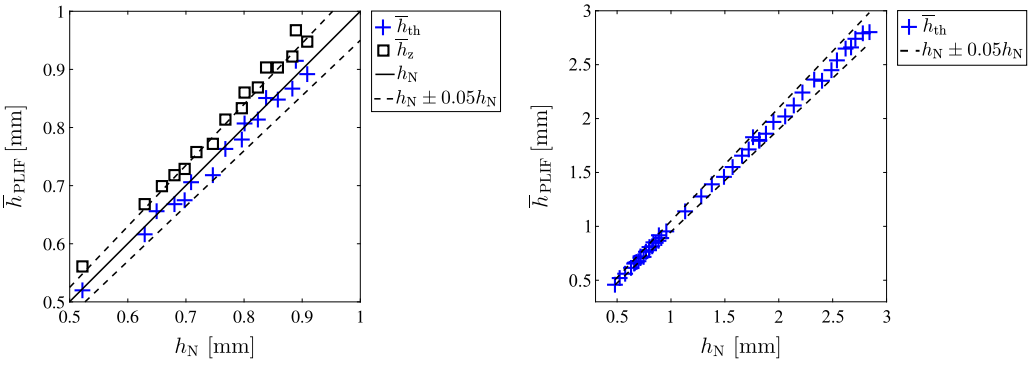

FIG. 5. Mean film-height data, $\overline{h}_{\rm PLIF}$, recovered by application of PLIF and plotted against corresponding Nusselt heights, $h_{\rm N}$, over the ranges (a) $h_{\rm N} \approx 0.5$–1 mm and (b) $h_{\rm N} \approx 0.5$–3 mm (reproduced from Fig. 4 in Ref. [11]).

interface. The second measurement set was obtained in order to scrutinize the sensitivity of the film-height measurement on the selected threshold level.

In Fig. 5(a), the mean film heights, $\overline{h}_{\rm th}$, that were recovered using $I_{\rm th} \neq 0$ are plotted alongside the mean film heights, $\overline{h}_z$, that were recovered using $I_{\rm th} = 0$, against their corresponding $h_{\rm N}$ over the range $h_{\rm N} = 0.5$–1 mm. The continuous and dotted lines represent $\overline{h}_{\rm PLIF} = h_{\rm N}$ and $\overline{h}_{\rm PLIF} = h_{\rm N} \pm 0.05h_{\rm N}$ (i.e., the error in the calculation of $h_{\rm N}$). The mean absolute deviations between $h_{\rm N}$ and $\overline{h}_{\rm th}$ and between $h_{\rm N}$ and $\overline{h}_z$ over the 16 examined film flows amount to 13 μm (1.7%) and 44 μm (5.8%) respectively. In contrast, the mean deviation between $h_{\rm N}$ and $\overline{h}_{\rm th}$ is equal to -7 μm (-1.1%), whereas the mean deviation between $h_{\rm N}$ and $\overline{h}_z$ is the same as before; hence, $\overline{h}_z$ overestimates $h_{\rm N}$ systematically. The $\overline{h}_{\rm th}$ results from all 45 examined film flows are plotted in Fig. 5(b) against their corresponding $h_{\rm N}$ values. The mean and mean absolute deviations amount to -6 μm (-0.6%) and 18 μm (1.4%) respectively. These results are very satisfactory, especially considering that the resolution of our optical arrangement corresponds to approximately twice this value ($\approx$38 μm/pixel).

An estimate of the film-height measurement error originating primarily from camera noise was obtained by calculating film-height standard deviations in flat-film runs. These amounted to approximately 10 μm, which for the thinnest film regions encountered in our experiments ($\approx$200 μm), correspond to deviations of $\approx$5%. Given a mean film height (for all cases with negative inclination) of approximately 1 mm, the average uncertainty associated with the instantaneous film-height measurement, which includes both camera noise and any uncertainties associated with the interface-identification procedures, is estimated at 3% at most.

C. Parameter space

Seven sets of experiments were conducted in total: four with the collection optics arranged to image a flow region extending $\approx$40 mm on either side of the middle of the film span and three with the collection optics arranged to image a flow region extending $\approx$48 mm inward from the film contact line, on the left-hand side of the test section. Each of the first four sets correspond to a different inclination angle and Ka combination; for the Ka = 330 film-flow experiments (49% glycerol by weight solution), $\beta = -15^\circ$, -30°, and -45°, whereas for the Ka = 13.1 film-flow experiments (82% glycerol by weight solution), $\beta = -30^\circ$. In the last three sets, Ka = 330, and $\beta = -15^\circ$, -30°, and -45°. The viscosity, $\nu_{\rm f}$, density, $\rho_{\rm f}$, and surface tension, $\sigma_{\rm f}$, of the two aqueous-glycerol solutions that were employed in our film-flow experiments were measured using a Poulten Selfe and Lee U-tube viscometer, an electronic scale, and an Attension Sigma 700 force

TABLE I. Liquid properties, flow rates, Re and Ka for the four sets of experiments performed with the collection optics arranged to image a region of the flow extending symmetrically about the middle of the film span.

β [deg]	ρ_f [kg m^{-3}]	ν_f [10^{-6} m^2 s^{-1}]	σ_f [10^{-3} N m^{-1}]	Q [10^{-5} m^3 s^{-1}]	Re	Ka
−15	1127 (±1)	4.4 (±3%)	57.7 (±2%)	2.2–15.5 (±3%)	19–133 (±3%)	330 (±4%)
−30	1214 (±1)	49.9 (±2%)	62.4 (±2%)	0.6–9.2 (±3%)	0.6–8.2 (±3%)	13.1 (±3%)
−30	1127 (±1)	4.4 (±3%)	57.7 (±2%)	2.2–20.5 (±3%)	21–193 (±4%)	330 (±4%)
−45	1127 (±1)	4.4 (±3%)	57.7 (±2%)	2.3–16.8 (±3%)	22–160 (±3%)	330 (±4%)

tensiometer, respectively. For this purpose, samples were collected throughout the duration of the optical measurements, and the results were averaged. The uncertainties that we quote in Table I for the liquid properties correspond to standard-deviation calculations based on five independent measurements (i.e., using five different liquid samples.)

The liquid flow rate and Re ranges for the first four measurement sets are depicted in Table I, alongside the liquid properties, while the same data for the last three measurement-sets are presented in Table II. Earlier, we noted that optical measurements were conducted while gradually reducing the flow Re by reducing the liquid flow rate all the way to the lowest setting which did not trigger any further film contraction. This was performed in increments of $\approx 0.5 \times 10^{-5}$ m^3 s^{-1}, which correspond to Re increments of ≈7 for the Ka = 330 flows and 0.7 for the Ka = 13.1 flows. The uncertainties quoted for the flow Re and liquid Ka are standard error calculations.

Finally, the film span at the PLIF imaging location, x_f, was recorded for each measurement set and is stated in Table III, along with the span of the dewetted regions on either side of the film, x_1 and x_2. The uncertainties quoted for these measurements are standard deviations calculated from data collected in independent, dedicated runs.

IV. TOPOLOGICAL OBSERVATIONS

A. Film flows with Ka = 13.1 and $\beta = -30°$

The interface topology of film flows with $\beta = -30°$, Ka = 13.1, and Re = 0.6 − 8.2 was discussed in a previous publication (see Ref. [11]), and therefore we only provide a brief synopsis of the main findings here for completeness and to facilitate the upcoming discussion on the topological features that were observed under different flow conditions. This discussion is further assisted by the presentation of spatiotemporal film-height maps, such as the one shown in Fig. 6, that are compiled over a 1-s recording period. The color scale corresponds to the film height, the y axis to the recording time, and the x axis to the distance along the imaged domain in the transverse (spanwise) direction of the flow. Atop each spatiotemporal film-height map, the local time-averaged film height, $\overline{h}_x$, is plotted along with the local film-height standard deviation, σ_x, which is represented by error bars. These statistical quantities should not be confused with the global mean film heights and film-height standard deviations, $\overline{h}$ and σ_h, respectively, which are calculated using all the available film-height data rather than film-height time series extracted from each location x along the imaged domain.

TABLE II. Liquid flow rates Re and Ka for the three sets of experiments performed with the collection optics arranged to image one side of the film, i.e., region extending from the contact line toward the center of the film.

β [deg]	Q [10^{-5} m^3 s^{-1}]	Re	Ka
−15	3.5–13.3 (±3%)	30–115 (±3%)	330 (±4%)
−30	3.5–17.0 (±3%)	33–159 (±4%)	330 (±4%)
−45	3.4–16.1 (±3%)	32–154 (±3%)	330 (±4%)

TABLE III. Film contraction data for the four sets of experiments carried out with the collection optics arranged to image a region of the flow extending symmetrically about the film span.

β [deg]	Ka	x_1 [10^{-3} m]	x_2 [10^{-3} m]	x_f [10^{-3} m]
−15	330	11 (±3)	12 (±3)	267 (±5)
−30	13.1	35 (±7)	28 (±7)	227 (±12)
−30	330	23 (±3)	22 (±3)	245 (±5)
−45	330	24 (±4)	25 (±4)	241 (±5)

At Re = 0.6, the film free surface is smooth and only populated by rivulets of near-equal amplitude [Fig. 6(a)]. A rivulet evolution scenario akin to the one proposed by Scheid *et al.* [44,45] for water films heated uniformly from the wall side could potentially account for the observed topology, with the cross-stream component of gravity (rather than the Marangoni effect) triggering the formation of rivulets upstream of the measurement location. At Re = 1.4, regular hydrodynamic waves of varying amplitude travel over the rivulet crests, but not the troughs [Fig. 6(b)]. Hence, as the local liquid flow rate increases, the local Re also increases, favoring the hydrodynamic instability mode [44,45]. Over the range Re = 1.4–3.5, the regular wave trains disintegrate into complex 3-D wave patterns, similar to those observed by Alekseenko and coworkers when investigating the formation of rivulets in water films falling down a vertical wall [36–38]. In greater detail, these authors reported the formation of forward protrusions separated by lagging "walls" on the crests of 2-D waves; as the protrusions overtook the walls, their wakes perturbed the trailing-wave crests and triggered a moderate redistribution of liquid along the transverse direction of the flow. In our experiments, the interface topology comprises strongly bent wave crests at Re = 2.1, which brake down into protrusions, flat-film layers, and walls over the range Re = 2.1–3.5 [see Figs. 6(c) and 6(d)]. The onset of stronger waviness in the rivulet troughs is evidenced by the locally higher σ_x values [Fig. 6(c)]. It should also be noted that despite the apparent random scatter of these waves over the liquid surface, the coherent film-height modulation along the cross-stream direction of the flow is preserved.

Over the range Re = 3.5–8.2, the flow experiences a progressive reorganization with solitary-wave sequences appearing and growing on the rivulet crests. The crest heights, trough heights, and periods of these waves fluctuate only modestly [Fig. 6(e)]. With increasing flow rate over the range Re = 4.3–8.2, the mean rivulet-crest heights and local standard deviations increase, while the rivulet-trough heights and local standard deviations fall. Based on these observations, we propose the onset of an inertia-dominated mechanism that "feeds" the rivulets with additional liquid mass, which is distributed according to the balance between inertia and gravity on the one hand and curvature (capillarity) on the other, which seeks to stabilize the flow.

B. Film flows with Ka = 330 and $\beta = -30°$

The interface topology of water-glycerol films with Ka = 330 and $\beta = -30°$ is examined over the range Re = 21–193. Spatiotemporal film-height maps are presented in Fig. 7 for flows with Re = 21, 36, 52, 67, 91, and 175, while $\overline{h}_x$ and σ_x, calculated along the PLIF imaged domain, are presented in Fig. 8.

At Re = 21 [see also Fig. 7(a)], the interface is populated by closely packed U/horseshoe-shaped and W-shaped waves, preceded by strongly bent capillary ripples and large, transversely modulated solitons that travel over a smooth substrate film. Numerous researchers have observed similar wave patterns and phenomena when investigating the 2-D to 3-D wave transition in conventional planar falling-films (e.g., see Refs. [17,25,28,35]). In particular, in Demekhin *et al.* [29–32], the authors reported horseshoe-like solitons with rounded fronts and Λ solitons (pointier and more elongated structures) at higher Re that slide over a slow-moving thin liquid substrate. Based on a Lagrangian

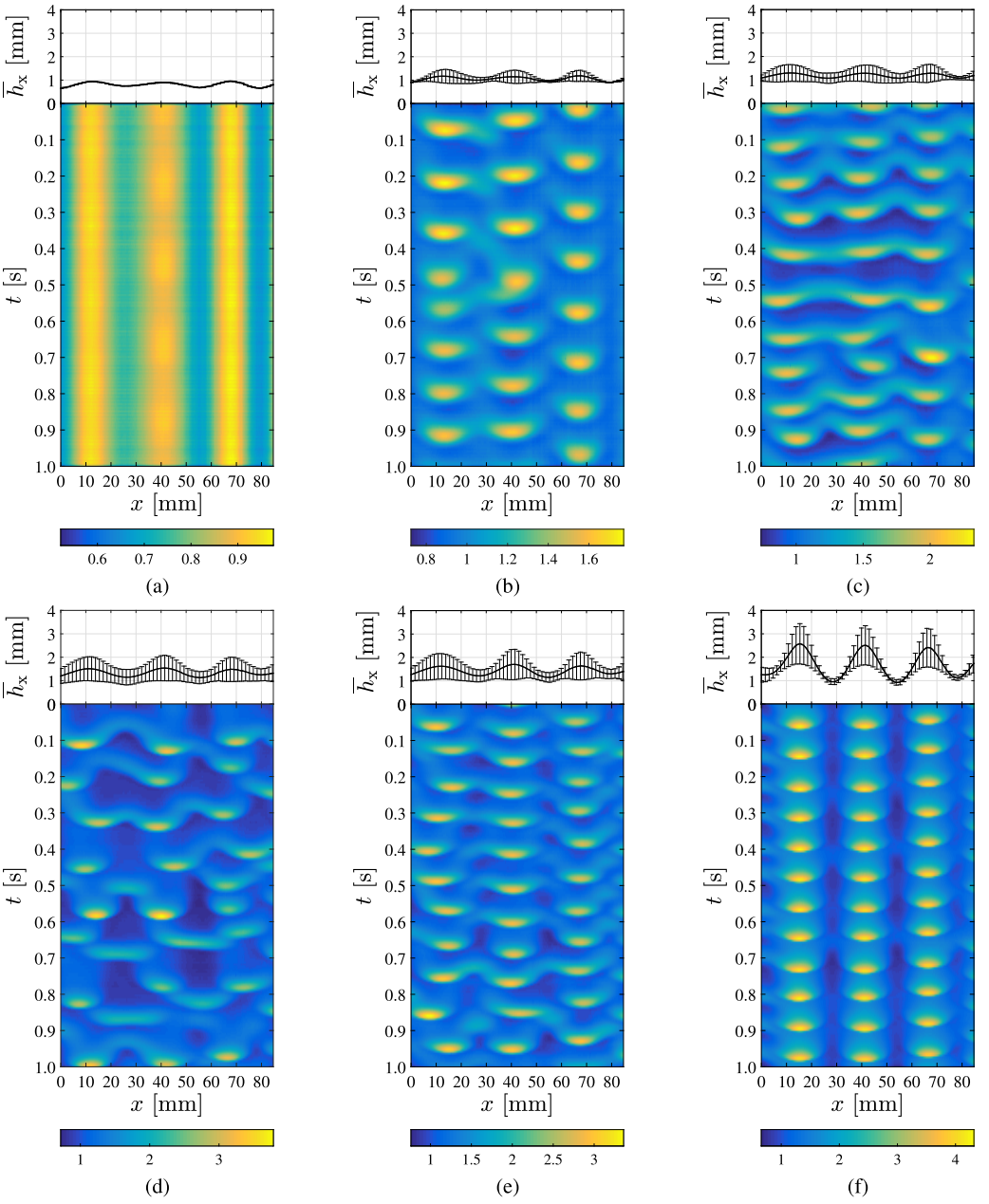

FIG. 6. Space- and time-resolved film-height measurements from flows with (a) Re = 0.6, (b) Re = 1.4, (c) Re = 2.1, (d) Re = 3.5, (e) Re = 4.3, and (f) Re = 8.2, in all cases for Ka = 13.1 and $\beta = -30^\circ$. This figure was reproduced from Fig. 5 in Ref. [11].

description of the flow, these authors linked the onset of surface turbulence to the tail overlap and coupling and continuous interaction between neighboring waves (similar to 2-D flows [67]).

In Fig. 9, we take a closer look at some of these interactions based on film-height data obtained at Re = 29 over a recording period of 0.35 s. The region marked "1" is preceded and trailed by pairs of protruding wavefronts (W-shaped waves); these, in turn, are preceded by capillary ripples that interfere and form a "checkerboard" pattern comprising clusters of dimples ahead of and in

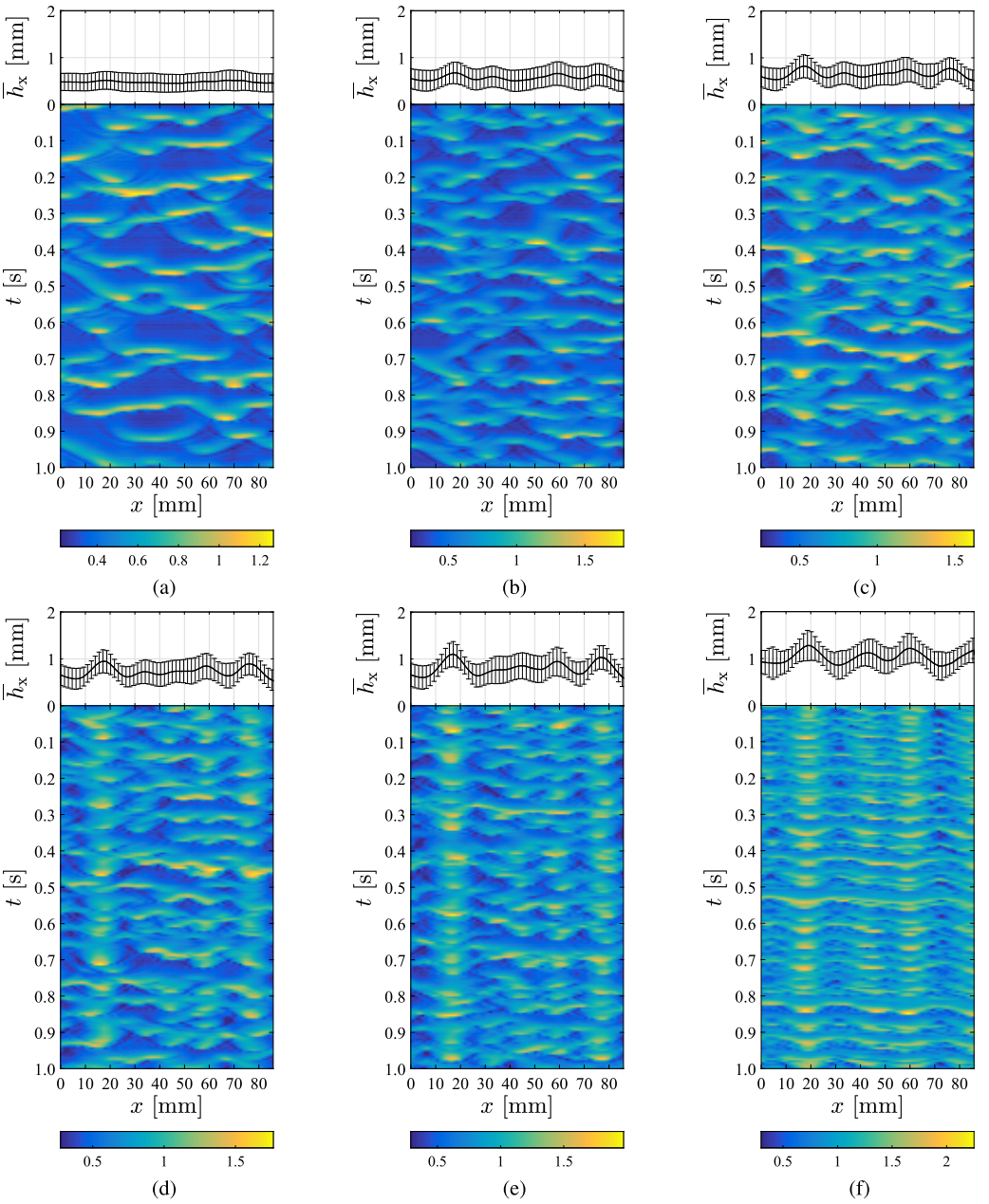

FIG. 7. Space- and time-resolved film-height measurements from flows with (a) Re = 21, (b) Re = 36, (c) Re = 52, (d) Re = 67, (e) Re = 91, and (f) Re = 175, in all cases for Ka = 330 and $\beta = -30^\circ$.

between the fronts of adjacent waves. Behind these interference patterns, we observe single valleys that separate the ridges of adjacent waves.

Park and Nosoko [34] investigated the interference of capillary ripples preceding U- and W-shaped waves in carefully designed experiments that allowed for controlled spatiotemporal perturbations to be imposed on vertically falling water films. They also reported that the oblique capillary ripples forming around the main-wave humps interfered with the straight capillary ripples that preceded the flat and shorter fronts between the horseshoe "legs." The ensuing clusters of

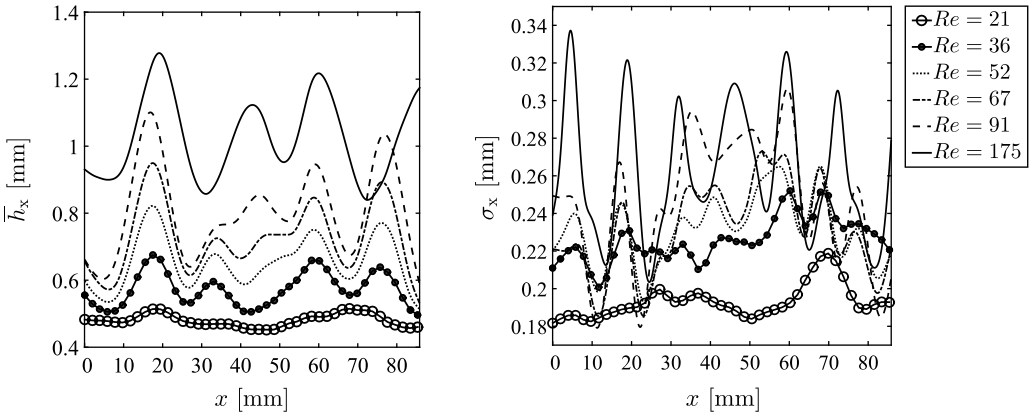

FIG. 8. (a) Space-resolved mean film-height, $\overline{h}_x$, and (b) film-height standard deviation, σ_x, calculated along the imaged domain for flows with Re = 21, 36, 52, 67, 91, and 175, in all cases for Ka = 330 and $\beta = -30^\circ$.

dimples decelerated and split off the legs, the height of the flat wavefronts gradually diminished, and the clusters disintegrated before the trailing waves caught up with them. Kofman *et al.* [26] also observed checkerboard patterns between the fronts of adjacent U-shaped waves, following the onset of transverse 3-D instabilities on 2-D solitary waves traveling on the surface of a water film. In their combined experimental-numerical study of the stability of quasisolitary waves, they attributed

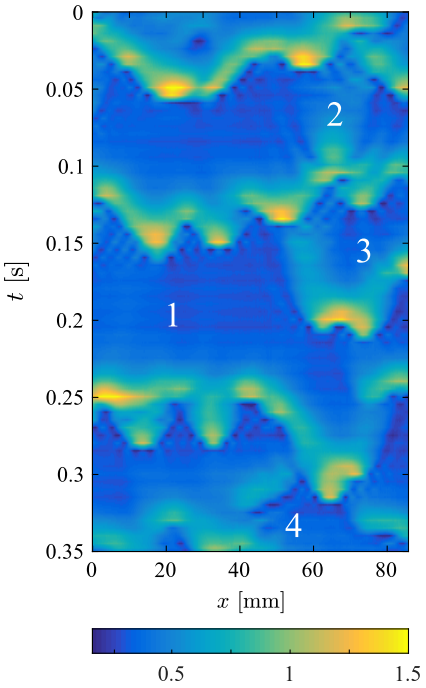

FIG. 9. Spatiotemporal film-height map compiled over a 0.35-s recording period from a flow with Re = 29, Ka = 330, and $\beta = -30^\circ$.

these formations, which they referred to as modulated "scallop waves," on the interaction between the capillary (short-wave) and inertial (long-wave) instability modes. The short-wave mode arises in the capillary regions of the quasisolitary waves with a mechanism akin to the R-T instability, producing regular arrays of rugged waves. These waves, observed for small inclination angles and ahead of the almost-undeformed crests of 2-D solitary waves, have a transverse wavelength that matched closely the length of the capillary ripples.

Three more regions relating to commonly observed interfacial features have been marked in Fig. 9. Region 2 shows bow-shaped capillary ripples extending along the sides of a U-shaped wave, 3 shows outward-radiating rows of depressions preceding a wave hump, and 4 shows a bow-shaped sequence of depressions. Bow-shaped capillary ripples and outward-radiating depressions are typically detected in relatively flat-film regions, and consequently such structures do not survive at higher Re where almost the entire film surface is covered by large-amplitude hydrodynamic waves. In contrast, both the checkerboard patterns and bow-shaped depression sequences (region 4) survive at higher Re [Figs. 7(c) and 7(d)]. The former are typically encountered in the rivulet troughs, while the latter are shown to extend on either side of fast-moving pulses that travel over the rivulets.

Over the range Re = 21–52, the interface topology changes significantly; the wide fronts which sometimes spanned the entire imaged domain brake down into smaller and faster pulses, whereas flat-film regions are now only rarely observed [see Figs. 7(b) and 7(c)]. Rivulets form already from Re = 36 and become progressively more pronounced, large-amplitude waves are encountered mainly along the rivulet crests, and the capillary wave patterns that were discussed earlier migrate to the rivulet troughs. Both $\overline{h}_x$ and σ_x increase with increasing Re (see Fig. 8); however, the former increases more by comparison, leading to lower film-height waviness as quantified by the relative standard deviation or coefficient of variation, $\sigma_x/\overline{h}_x$, over the same Re range. Increasing the flow Re further, first to Re = 67 and then to Re = 91, accentuates the disintegration of any wide and heavily curved fronts into smaller and more frequent individual pulses [see Figs. 7(c)–7(e)]. Interestingly though, the intermittent passage of quasi-2-D waves that extend along the entire imaged domain persists over the same flow Re and results in appreciable liquid-mass transport across the rivulet troughs. At higher Re, for example, at Re = 175 [see Fig. 7(f)], the liquid surface is covered in such quasi-2-D waves.

From the mean film-height data presented in Fig. 8(a), it can be observed that the disparity between the rivulet crest and trough heights relative to the overall mean film-height increases between Re = 36 and Re = 92 and then decreases. This implies that with increasing inertia above Re $\approx$ 90, a smaller portion of the liquid mass flow is directed into the rivulets crests, unlike what was observed in the range Re = 29–52. It is therefore possible to assume that the rivulet amplitude is maximized inside the range Re = 90–175 and that any increase in the mean-flow Re beyond this point suppresses further a increase of the rivulet amplitude. We expect this transition to be inclination-angle dependent, such that for a larger negative inclination the suppression of the rivulet amplitude should necessitate a stronger inertial contribution and should thus appear at higher Re, whereas for a smaller negative inclination, a lower Re should suffice in moderating the amplitude of the rivulets. Both hypotheses are discussed later in this paper, when the topologies of films inclined at $\beta = -45^\circ$ and $\beta = -15^\circ$ are considered, as well as in the last section where we discuss our film-height measurements in detail. Finally, with increasing Re, the distance between adjacent rivulet crests and troughs increases [see Fig. 8(a)], in agreement with the results of Kharlamov *et al.* [38].

C. Film flows with Ka = 330 and $\beta = -45^\circ$

The interface topology of Ka = 330 films inclined at $\beta = -45^\circ$ was investigated over the range Re = 22–160. Below Re $\approx$ 30, no rivulets are observed and the film free surface is populated by continuously interacting U- and W-shaped solitary pulses and transversely modulated quasi-2-D waves [see Fig. 10(a)]. Also similar to the low-Re, $\beta = -30^\circ$ case that was examined earlier, interfacial features such as checkerboard patterns, bow-shaped capillary waves, outward-radiating

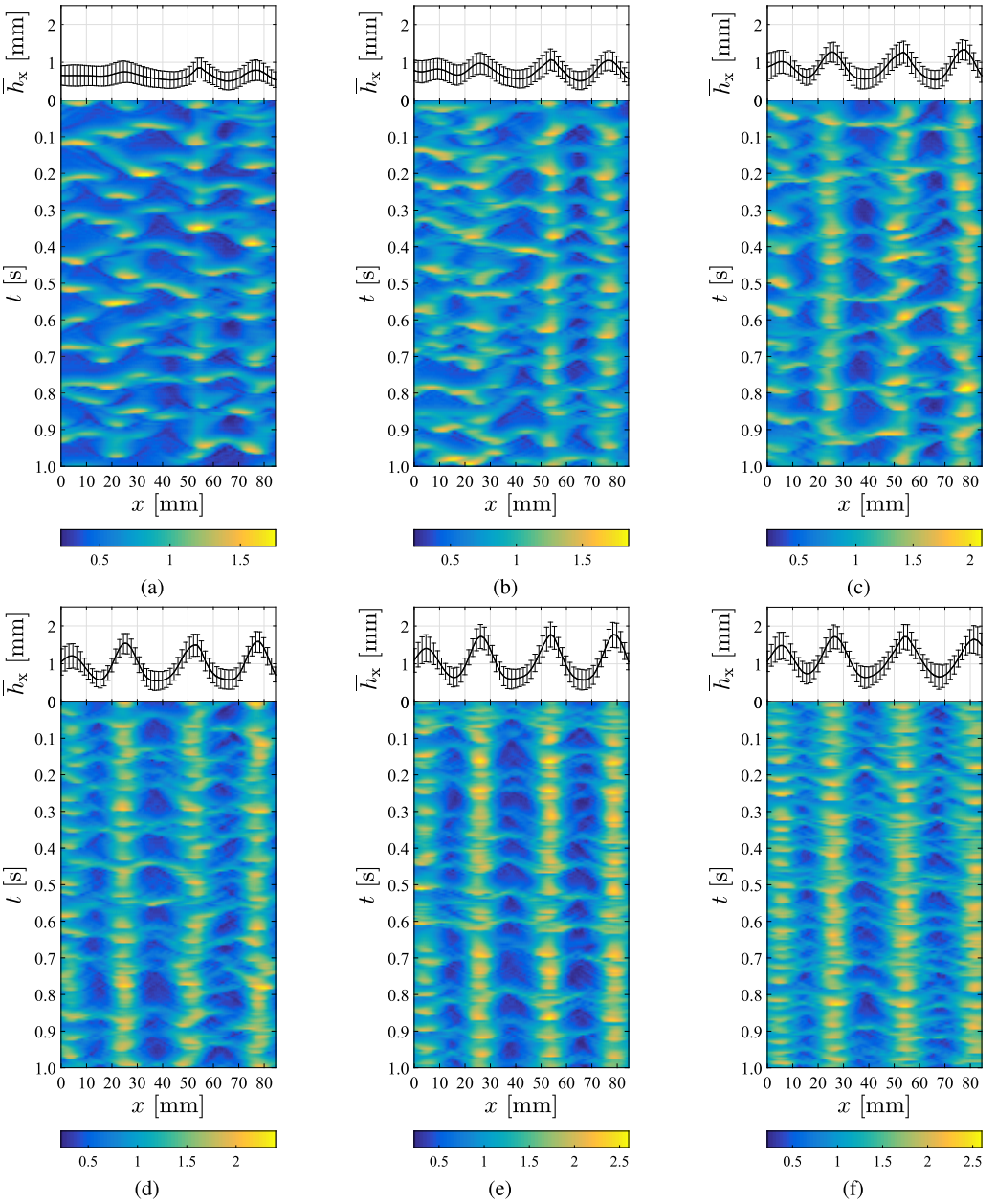

FIG. 10. Space- and time-resolved film-height measurements from flows with (a) Re = 38, (b) Re = 60, (c) Re = 86, (d) Re = 110, (e) Re = 138, and (f) Re = 160, in all cases for Ka = 330 and $\beta = -45^\circ$.

rows of depressions and bow-shaped sequences of depressions are encountered. Between Re $\approx$ 30 and Re $\approx$ 60, however, the increase of the rivulet amplitude is more pronounced than before; based on the $\overline{h}_x$ data presented in Figs. 8(a) and 11(a), the rivulet amplitude (mean difference between the rivulet trough and crest heights) increases from 0.12 to 0.22 mm between Re = 36 and Re = 67 when $\beta = -30^\circ$, while when $\beta = -45^\circ$, the same quantity increases from 0.28 mm at Re = 38 to 0.43 mm at Re = 60. In fact, the data plotted in Fig. 11(a) for Re = 38 and 60 reveal that almost all the additional liquid flow that is introduced by increasing the mean flow rate is channeled

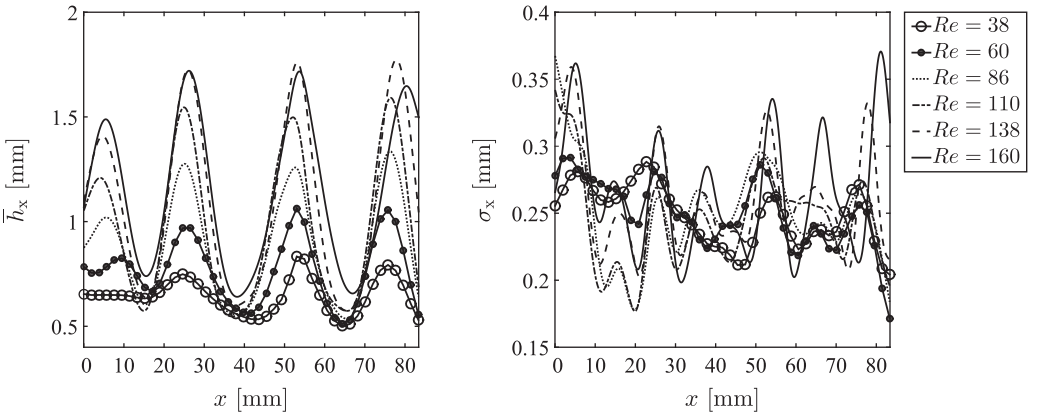

FIG. 11. (a) Space-resolved mean film height, $\overline{h}_x$, and (b) film-height standard deviation, σ_x, calculated along the imaged domain for flows with Re = 38, 60, 86, 110, 138, and 160, in all cases for Ka = 330 and $\beta = -45^\circ$.

through the rivulets. In contrast, any additional liquid flow is more evenly distributed along the film span over the same Re range when $\beta = -30^\circ$ [see Fig. 8(a)]. A possible explanation for this disparity is that as the wide, quasi-2-D waves that are observed at low Re break down into smaller and faster moving pulses with increasing inertia, they gain mass and grow faster when $\beta = -45^\circ$ due to the stronger cross-stream gravitational pull. It should also be noted that the near-constant distance between adjacent rivulet crests and troughs could result, in part, from the way the flow Re is varied in this study (i.e., from high to low values), such that the wavelength that is observed at the highest Re is also preserved at lower Re, as if it was triggered by finite-amplitude perturbations rather than infinitesimal perturbations. The variation of the rivulet wavelengths with both the flow Re and the inclination angle β is discussed in greater length in the last section of this paper, along with any dependencies of these results on features that are specific to our experimental configuration, including the noise spectrum of our experiment and the limited span of the examined film flows at the location where we conduct our measurements relative to the observed rivulet wavelengths.

Increasing the flow Re further, first to Re = 86 and then to Re = 110, 138, and 160 [see Figs. 10(c)–10(f)], triggers the intermittent passage of wide, quasi-2-D wavefronts. This phenomenon is less prominent than before; such waves appear less frequently and the amplitudes of any individual pulses racing down the rivulet troughs lay considerably lower than those riding the rivulet crests. The rivulet amplitude increases until Re $\approx$ 138 and then decreases as the rivulet-trough height starts increasing with the rivulet-crest height. Earlier we attributed the suppression of rivulets at high Re to the drainage of liquid away from the rivulets and into the rivulet troughs and suggested that such a transition should be inclination-angle dependent. Despite the fact that a more detailed analysis is needed to accurately identify the Re above which the rivulet amplitude diminishes, based on the results presented so far in this work, it appears that a considerably stronger inertial contribution (i.e., a substantially higher Re) is not required in order to arrest rivulet growth when $\beta = -45^\circ$. The rivulet amplitude has, however, increased considerably compared to the $\beta = -30^\circ$ case, before decreasing at higher Re. It is also worth noting that the rivulet structures appear to "invade" the imaging domain from the edge to the right (the rivulets on the right-hand side display larger amplitudes than those on the left), in accordance with the description by Balestra *et al.* [68]. The latter have demonstrated experimentally that in the case of a thin liquid film coating the inner surface of a cylinder whose axis is set up at right angles to gravity, rivulets form first at the boundaries of the cylinder where the film is perturbed by the existence of a meniscus or contact

line. Thus, the R-T instability propagates from the boundaries, and the rivulet amplitude decreases near the center the domain.

Referring to Fig. 11(b), we observe that σ_x increases modestly compared to $\overline{h}_x$ between Re = 38 and Re = 60. This result suggests that the formation and growth of rivulets contributes toward a reduction in the overall film-height waviness over this Re range, such that the coefficient of variation of the film height indeed decreases from 0.41 to 0.38. The same conclusion relates to the Re = 138–160 data. Finally, a marked difference between the flow behavior observed here, and earlier when $\beta = -30^\circ$, is that whereas in the former case the distances between adjacent rivulet crests and troughs increased with the flow Re, these appear to be almost constant for the $\beta = -45^\circ$ flows and near equal to those observed at high Re for $\beta = -30^\circ$. This result can potentially be attributed to the merging of neighboring rivulets upstream of the imaged domain.

D. Film flows with Ka = 330 and $\beta = -15^\circ$

Our final measurement set relates to Ka = 330 films inclined at $\beta = -15^\circ$, and investigated over the range Re = 19–133. Instantaneous and local film-height maps are presented in Fig. 12 for Re = 19, 40, 61, 83, 108, and 133 films, and $\overline{h}_x$ and σ_x results are provided in Fig. 13. At Re = 19, the liquid flow is distributed evenly along the film span [Fig. 13(a)] and the observed waves display a pronounced 2-D character, extending along large sections of the imaged domain. Temporal flow profiles reveal highly asymmetric pulses with long, flat tails and steep fronts preceded by capillary ripples, resembling closely the profiles of 2-D solitary waves. The crest heights of these waves occasionally exceed the substrate-film height by a factor of ≈2. Increasing the flow Re to 40 and then to 61 triggers the formation of low-amplitude rivulets, while faster pulses and fronts race down the film and any flat-film regions become short-lived [Figs. 12(b) and 12(c)]. Interestingly, any large-amplitude waves appear to be randomly scattered across the film instead of congregating at the rivulet crests, while the flatter and thinner film regions and capillary-wave interference patterns are consistently encountered along the rivulet troughs. Despite the fact that the rivulet amplitudes are lower than those observed when $\beta = -30^\circ$ (Re = 44 and 60 flows), the obtained σ_h are, in fact, slightly higher for the same flow Re. Finally, the flow maps depicted in Figs. 12(d)–12(f) for Re = 83, 108, and 133, reveal wide, quasi-2-D fronts that extend along the entire imaged domain and protrude marginally at the rivulet crests. The strongly bent capillary ripples that typically envelope the forward protrusions riding the rivulets, as well as the clusters of dimples that populated the rivulet troughs at lower Re, have evolved into isolated depressions and smaller groups of dimples. Over the range Re = 100–133, large-amplitude hydrodynamic waves are encountered over both the rivulet crests and troughs.

The data presented in Figs. 8(a) and 11(a) suggest that the rivulet-crest height increased more than the rivulet-trough height, at least for Re ⩽ 91 and Re ⩽ 86 when $\beta = -30^\circ$ and $\beta = -45^\circ$, respectively; in contrast, for $\beta = -15^\circ$, the mean rivulet-crest and trough heights increase almost in proportion to each other. Earlier we discussed the suppression of rivulet growth past some Re value, which we attributed to liquid drainage away from the rivulet crests and into the troughs. Even though this behavior was evident in Figs. 8(a) and 11(a), the $\overline{h}_x$ data presented in Fig. 13(a) for $\beta = -15^\circ$ do not, at first glance, reveal such a behavior. This finding suggests that once the rivulets are formed at Re ≈ 40, the introduction of any additional liquid mass (by increasing the mean flow rate) is not channeled preferentially along the rivulet crests but is transported through the inter-rivulet regions. Our statistical results (presented in Sec. VI), however, imply that the same transition does occur at ≈Re = 80, but it is less prominent compared to the $\beta = -30^\circ$ and $\beta = -45^\circ$ flows.

V. TOPOLOGICAL OBSERVATIONS NEAR THE LATERAL RIM OF THE FILM

As stated earlier, a further series of film-height measurements was also conducted for films with Ka = 330 and $\beta = -15^\circ$, -30°, and -45°, in a region of the flow extending ≈45 mm inward from the film-contact line on the left-hand side of the test section (the center of the film span is located ≈110–135 mm away from the contact line, depending on the inclination angle). Near the

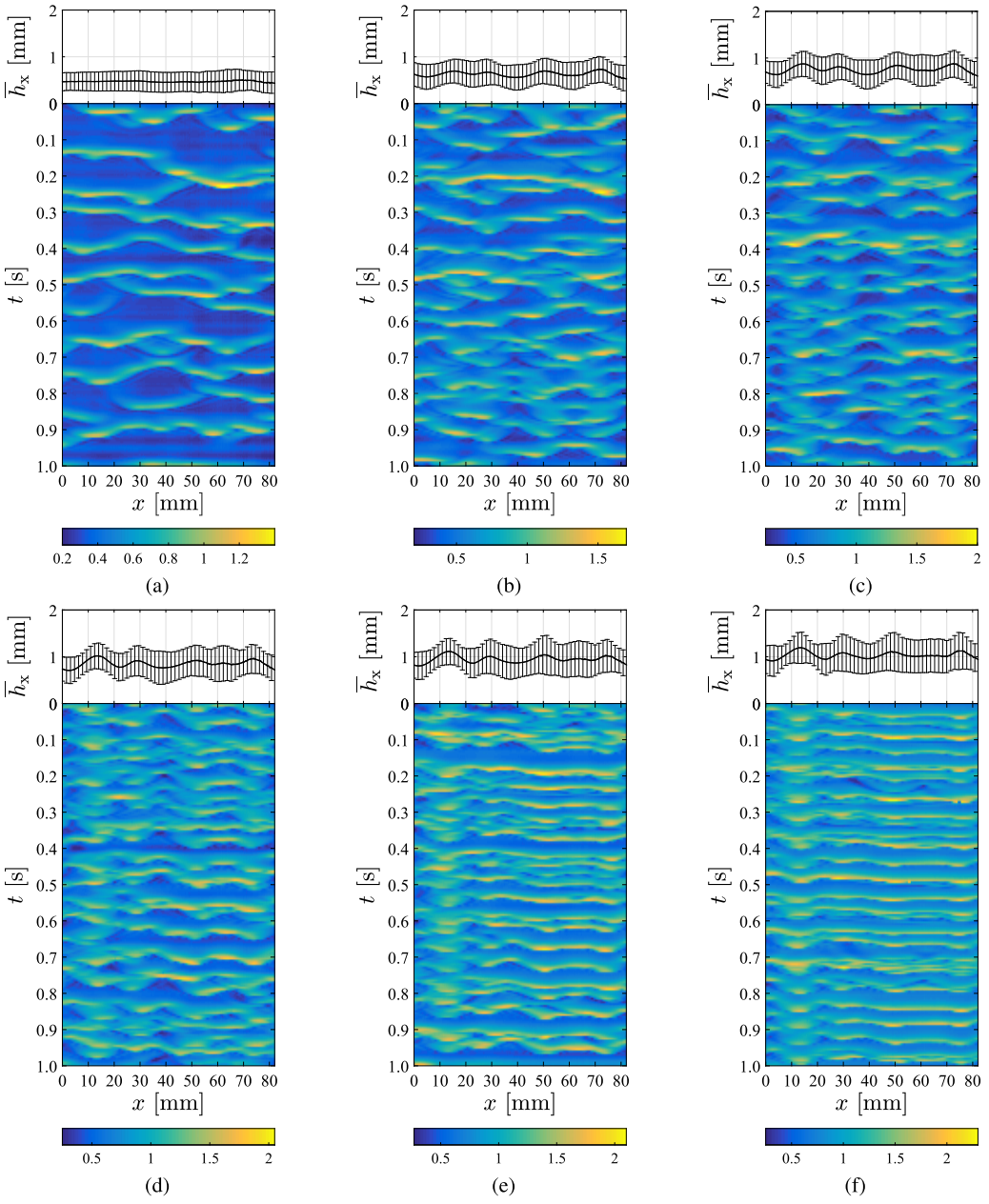

FIG. 12. Space- and time-resolved film-height measurements from flows with (a) Re = 19, (b) Re = 40, (c) Re = 61, (d) Re = 83, (e) Re = 108, and (f) Re = 133, in all cases for Ka = 330 and $\beta = -15^\circ$.

contact line, the film is bounded by a rivulet that exceeds in height any adjacent rivulets, as well as any rivulets observed about the middle of the film span. This rivulet, which we henceforth refer to as the lateral rim of the film, has appeared in several investigations focusing on the shrinkage characteristics of heated falling films, and its emergence has been linked to the formation of rivulets via the thermocapillary-instability mechanism (see, for example, Refs. [47,48]).

When $\beta = -15^\circ$ and Re = 30 [see Fig. 14(a)], the film region adjacent to the lateral rim ($x \approx$ 20–50 mm) is devoid of rivulets. Hydrodynamic waves travel over the rim, and the local film-height

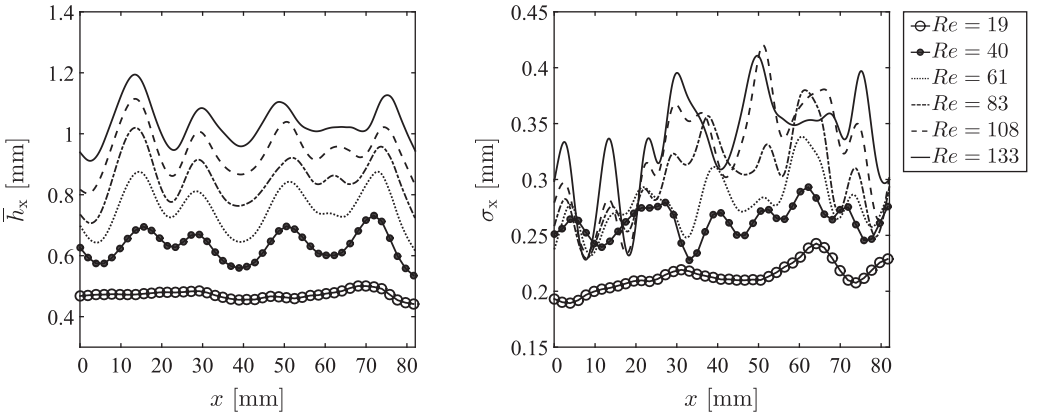

FIG. 13. (a) Space-resolved mean film-height, $\overline{h}_x$, and (b) film-height standard deviation, σ_x, calculated along the imaged domain for flows with Re = 19, 40, 61, 83, 108, and 133, in all cases for Ka = 330 and $\beta = -15^\circ$.

standard deviations match those from the remainder of the imaged domain. With increasing Re, first to Re = 85 and then to Re = 115, low-amplitude rivulets emerge, and the observed wave patterns resemble those presented in Figs. 12(d) and 12(e). Interestingly, as the rim height increases, the local standard deviation decreases (the film-height standard deviations at the rim crests are indicated as blue error bars); in contrast, the film-height standard deviations along the rest of the imaged domain, including the rim trough, increase (shown as black error bars). It is also worth noting that as the flow Re increases, the width of the lateral rim increases modestly, and its trough moves away from the contact line. The angle formed between the lateral rim and the substrate increases with increasing flow Re, from $\theta \approx 10^\circ$ at Re = 30, to 12.6°, 14.5°, and 16.2° at Re = 58, 85, and 115 respectively. Using liquid samples that were collected during our experiments, the equilibrium contact angle of the 49% glycerol by weight aqueous solution was measured on soda-lime glass with the sessile drop method and corresponds to 36.8°. The contact angle measurements were conducted at the same temperature as the film-flow experiments (i.e., 25 °C).

In the case of the $\beta = -30^\circ$ and Re = 33 flow, the rim crest lies higher and its trough lies lower compared to the $\beta = -15^\circ$ and Re = 30 flow. The topology of the adjacent film-region (i.e., for $x \geqslant 20$ mm) exhibits a less pronounced modulation in comparison to the Re = 36 flow that is presented in Fig. 7(b), as more liquid is transported locally by the lateral rim [see Fig. 14(b)]. Moreover, unlike the case with $\beta = -15^\circ$, the flow at the rim crest exhibits almost no fluctuations at all, while the trough height fluctuates only modestly compared to the rest of the imaged domain. With increasing flow Re, first to Re = 95 and then to Re = 159, the intermittent passage of larger hydrodynamic waves over the rim induces some fluctuations locally which are, however, small compared to the rest of the imaged domain, including the rim trough itself. The crest height of the rivulet that has emerged in close vicinity to the lateral rim matches the height of the rivulets observed near the middle of the film span [Fig. 7(d)] but is still only about half as high as the lateral rim, which measures 1.96 mm at Re = 95 and 2.42 mm at Re = 159. The angle between the lateral rim and the substrate increases from $\theta = 14.1^\circ$ at Re = 33, to 19.5°,22.4°, 24.2°, and 25.6° at Re = 64, 95, 124, and 159, respectively.

Finally, when the inclination angle is set to $\beta = -45^\circ$ and the flow Re is varied between Re = 32, 93, and 154, topologies akin to the $\beta = -30^\circ$ cases are observed; the rivulet amplitudes are, however, even larger for the same flow Re. The lateral-rim crest height increases from 1.28 to 1.99 mm and then to 2.70 mm over the investigated Re range, while the rim-trough height diminishes slightly, measuring 0.40, 0.34, and 0.32 mm, respectively. The crest height of the second rivulet

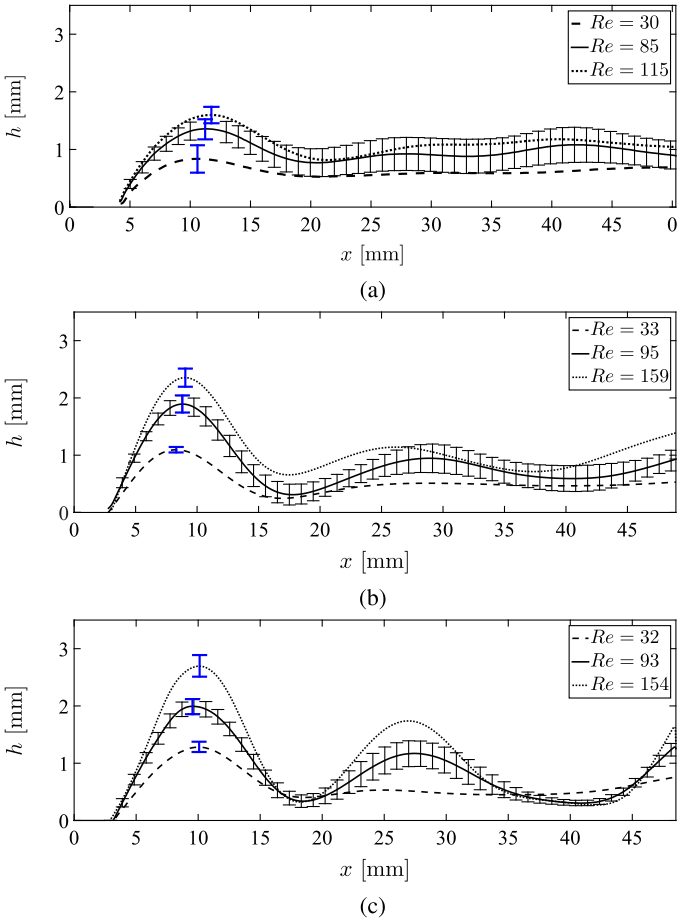

FIG. 14. Space-resolved mean film height, $\overline{h}_x$, and film-height standard deviation, σ_x, calculated along the imaged domain for flows with (a) Re = 30, 85, and 115, for Ka = 330 and $\beta = -15^\circ$, (b) Re = 33, 95, and 159, for Ka = 330 and $\beta = -30^\circ$, and (c) Re = 32, 93, and 154, for Ka = 330 and $\beta = -45^\circ$.

shown in Fig. 14(c) increases from 0.53 to 1.17 mm and finally to 1.74 mm, nearly matching the rivulet-crest heights that were measured about the middle of the film span (i.e., ≈0.7, 1.3, and 1.7 mm for Re = 30, 95, and 155 respectively). The film-height standard deviations at the lateral-rim crest increase modestly with the flow Re, in the same manner as in the $\beta = -30^\circ$ cases. The measured angles also match closely those obtained with $\beta = -30^\circ$, and correspond to $\theta = 14.1^\circ$, 17.5°, 21.4°, 25.5°, and 27.8° at Re = 32, 65, 93, 127, and 154, respectively. A plot of all measured θ values against their respective rim-crest heights is presented in Fig. 15, showing a linear relation between the two datasets. The data were fitted with a first-order polynomial which was forced through the origin, with a coefficient of determination of $R^2 = 0.97$. The slope of the fit corresponds to $\approx 11^\circ/\text{mm}$.

The influence of the lateral rim on the film flow is unclear at this stage of our experimental campaign, and further research is required in order to better appreciate its role. In experiments carried out in falling films bounded by side walls, for example, the side-wall boundary condition involves strong shear effects which result in traveling waves that do not retain a flat crestline but instead become symmetrically curved about the middle of the film span. The strong crestline curvature observed by Georgantaki *et al.* [69] was attributed to the prevalence of capillary over

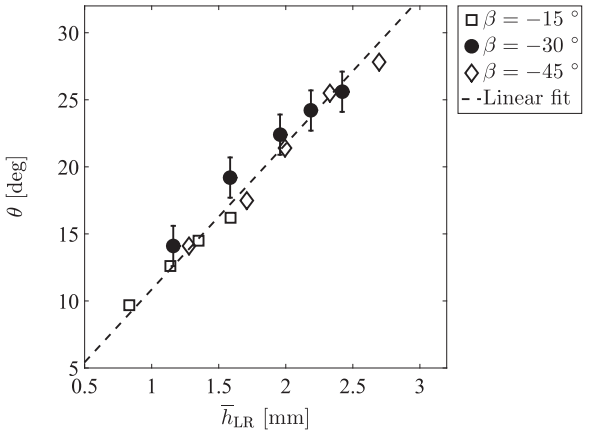

FIG. 15. Measured contact angle, θ, as a function of the lateral-rim crest height, $\overline{h}_{\mathrm{LR}}$, for all examined flow conditions.

viscous forces. When the contact angle between the liquid and the side wall is smaller than 90°, a velocity (and local Re) overshoot ensues as a result of capillary elevation. However, according to Pollak *et al.* [70], the destabilizing effect of the Re overshoot is of relatively short range compared to the stabilizing effect of the side walls. In our experiments, a contact line is found at the film boundary instead of a side wall. The flow adjacent to the contact line must accommodate the change from a constant slope to the film surface [see, for example, Fig. 14(a)], resulting in an overshoot in both the local film height and velocity (i.e., the lateral rim). Increasing the (flow) Re implies that a larger film thickness needs to be accommodated, which will amplify the deformation (i.e., increase the contact angle). Increasing β (i.e., imposing a larger negative inclination), and therefore the destabilizing gravity component, also increases the height of the suspended rim as well as the measured contact angle. The interdependence between the flow Re, β, the rim height, and the contact angle is captured in Fig. 15 for the examined film-flow conditions.

VI. QUANTITATIVE FILM-HEIGHT CHARACTERIZATION

A. Probability density functions

Film-height statistics were generated by selecting randomly 25 film-height data points from each image pair without replacement. The obtained datasets were first employed in generating film-height probability density functions (PDFs) such as the ones shown in Fig. 16, which span flow conditions across the four Re ranges that were investigated for each liquid Ka and β combination. We commence the analysis by first considering the results relating to flows with Ka = 330. Below Re $\approx$ 30, all PDFs exhibit the typical shape and characteristics that have been reported by numerous investigators for falling-film flows at low Re (see, for example, Refs. [8,71,72]). These include a sharp peak (in this case at $h = 0.33$ mm for $\beta = -15°$ and $-30°$ and at $h = 0.35$ mm for $\beta = -45°$), which represents the substrate-film height, and a strongly skewed shape due to the intermittent passage of large-amplitude waves. As the flow Re increases above Re $\approx$ 60, the modes of the PDFs shift to higher values ($h \approx 0.48$ mm for $\beta = -15°$, $h \approx 0.75$ mm for $\beta = -30°$, and $h \approx 0.73$ mm for $\beta = -45°$) and the maximum-probability values drop, as large-amplitude waves are observed more frequently. Unlike liquid films flowing over inclined or vertical substrates that exhibit PDFs that remain skewed toward the substrate-film side even at very high Re (i.e., even under transitional or even turbulent flow conditions), the formation and growth of rivulets over the remainder of the investigated Re ranges triggers a pronounced "swelling" (skewness) in large sections of the PDFs to the right of the main peaks, resulting in more symmetric shapes. This

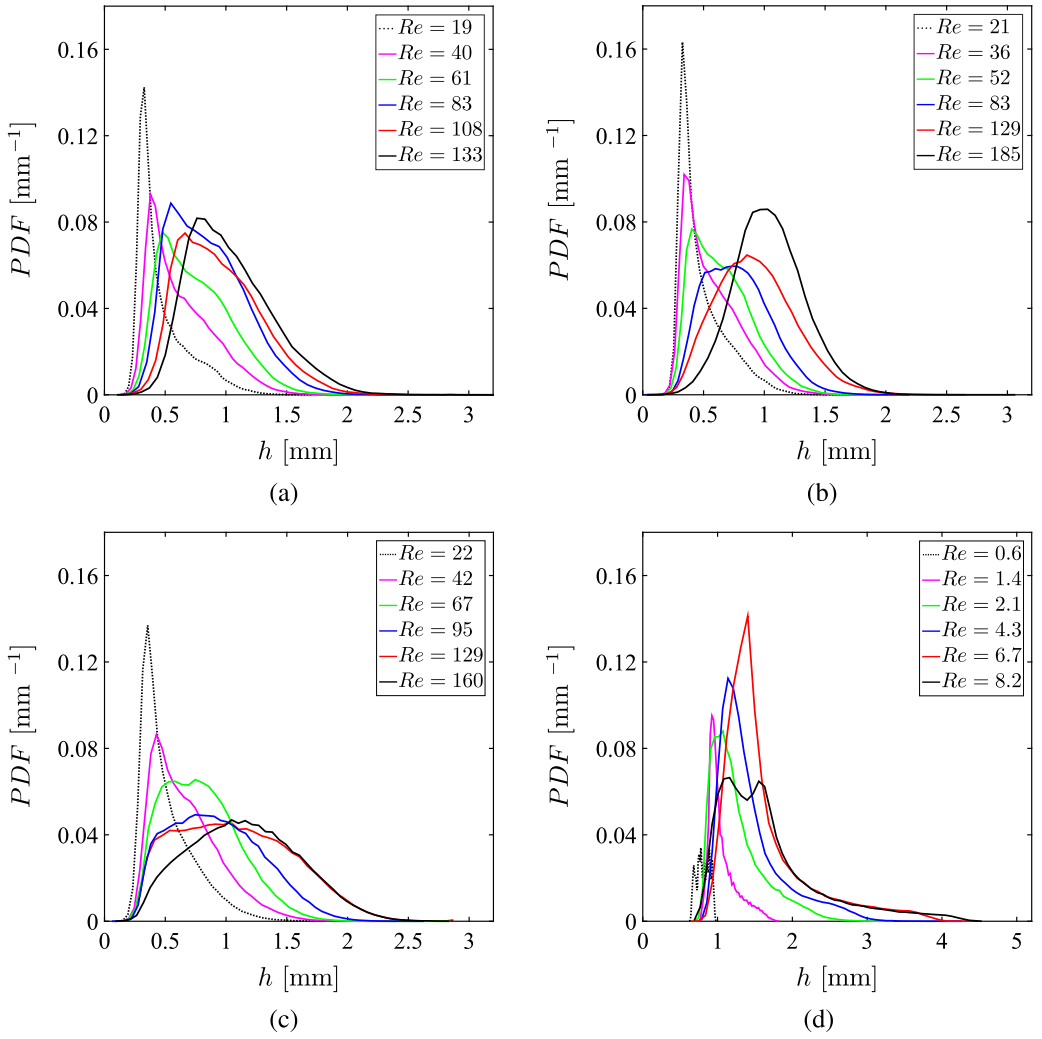

FIG. 16. Film-height PDFs for flow conditions spanning the four Re ranges that were investigated, each corresponding to a different liquid Ka and β combination. (a) Ka = 330, $\beta = -15^\circ$, (b) Ka = 330, $\beta = -30^\circ$, (c) Ka = 330, $\beta = -45^\circ$, and (d) Ka = 13.1, $\beta = -30^\circ$.

effect is more pronounced in the $\beta = -45^\circ$ flows, followed by the $\beta = -30^\circ$ flows, and finally the $\beta = -15^\circ$ flows; in the same order that rivulets become more prominent. Above Re $\approx$ 80 and all the way to Re $\approx$ 130, the PDFs generated using the $\beta = -15^\circ$ data display progressively reduced skewness, while for the $\beta = -30^\circ$ and $\beta = -45^\circ$ flows, the PDFs generated at Re = 185 and Re = 160, respectively, resemble closely Gaussian distributions. The modes of the distributions at the highest investigated Re (i.e., at Re = 133 when $\beta = -15^\circ$, Re = 185 when $\beta = -30^\circ$, and Re = 160, when $\beta = -45^\circ$) correspond to $h \approx 0.77$ mm, $h \approx 1.03$ mm and $h \approx 1.05$ mm respectively. These film-height values do not represent the substrate film anymore, and instead match closely the mean film heights.

In reference to the PDFs presented in Fig. 16(d) for flows with Re = 0.6–8.2, Ka = 13.1, and $\beta = -30^\circ$, some interesting observations can also be made. When Re = 0.6, the distribution is very narrow owing to the lack of hydrodynamic waves, and three distinct peaks are identified: one at $h = 0.68$ mm corresponding to the rivulet troughs, one at $h = 0.78$ mm corresponding to film

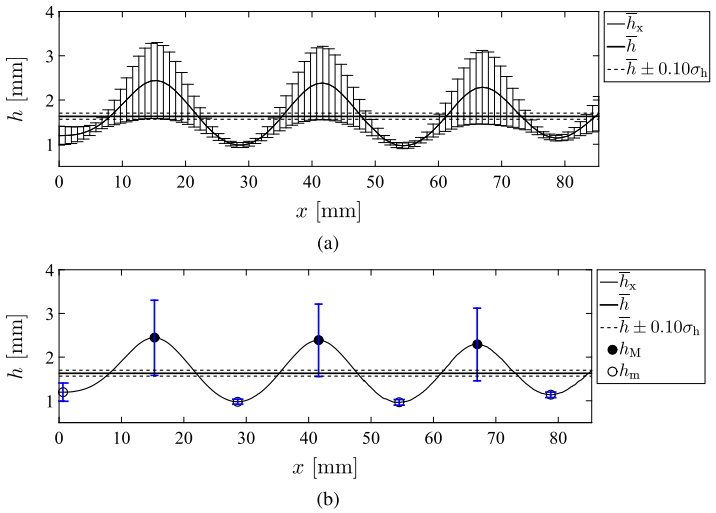

FIG. 17. (a) Mean film height, $\overline{h}_x$, and film-height standard deviation, σ_x, plotted as a function of the distance, x, along the imaged region of the flow for a film with Re = 8.2, Ka = 13.1, and $\beta = -30^\circ$; σ_x data are shown as error bars. (b) Same plot as in panel (a) but showing the location of the rivulet crests, $\overline{h}_M$, and troughs, $\overline{h}_m$, and the local standard deviations, $\sigma_{h,M}$ and $\sigma_{h,m}$, respectively; the last two are shown as error bars.

regions between the crests and troughs, and one at $h = 0.90$ mm corresponding to the rivulet crests. As the regular wave trains observed at Re = 1.4 give way to complex 3-D wave patterns over the range Re = 1.4–3.5, and then re-emerge at Re = 4.3, the relevant PDFs become strongly skewed to the left (i.e., toward low film-height values) and exhibit sharp peaks at $h = 0.92$ mm, $h = 1.07$ mm, and $h = 1.14$ mm for Re = 1.4, 2.1, and 4.3 respectively, which are representative of the substrate-film height. With increasing Re over the same range, the PDFs also widen considerably as large-amplitude solitary pulses pass by more frequently. Interestingly, between Re = 6.7 and Re = 8.2, the single sharp peak is replaced by a pair of peaks at $h = 1.16$ mm and $h = 1.55$ mm. The former coincides with the mean film height at the rivulet troughs, which exhibit very limited waviness (see Ref. [11]) and the latter with the substrate film along the rivulet crests. The resulting PDF thus comprises two overlapping PDFs, one describing the flow along the rivulet troughs and one describing the flow along the crests.

B. Mean film heights and film-height standard deviations

Mean film height, $\overline{h}$, and film-height standard deviation, σ_h, data are presented in Figs. 18 and 20 for all investigated flow conditions. Furthermore, beyond these statistics that were generated by selecting data points from the entire imaged flow regions, mean and standard-deviation data were also generated for flow regions corresponding to the rivulet crests and troughs alone, denoted by $\overline{h}_M$ and $\overline{h}_m$, and $\sigma_{h,M}$ and $\sigma_{h,m}$, respectively. Prior to commencing our discussion of the relevant results, we first outline the procedure that we followed in order to identify the spanwise coordinates that correspond to the rivulet crests and troughs, which was required for this analysis. After calculating $\overline{h}$ and σ_h over the entire imaged flow span and all images (time), we then obtained the same quantities over time, as a function of distance, x, along the imaged region of the flow, $\overline{h}_x$ and σ_x (see Figs. 6, 7, 10, and 12). We then used threshold values, $\overline{h} \pm 0.10\sigma_h$, to derive boundaries about $\overline{h}$ (see, for example, Fig. 17(a) for a flow with Re = 8.2, Ka = 13.1, and $\beta = -30^\circ$). When $|\overline{h}_x - \overline{h}| \leqslant \overline{h} + 0.10\sigma_h$ and depending on whether $\overline{h}_x - \overline{h}$ is positive or negative, we interpret the local film regions to belong to either a rivulet crest ($\overline{h}_x - \overline{h} > 0$) or a trough ($\overline{h}_x - \overline{h} < 0$). Next, we identify the local extrema (i.e., minima or maxima), and generate time series from which $\overline{h}_M$, $\overline{h}_m$,

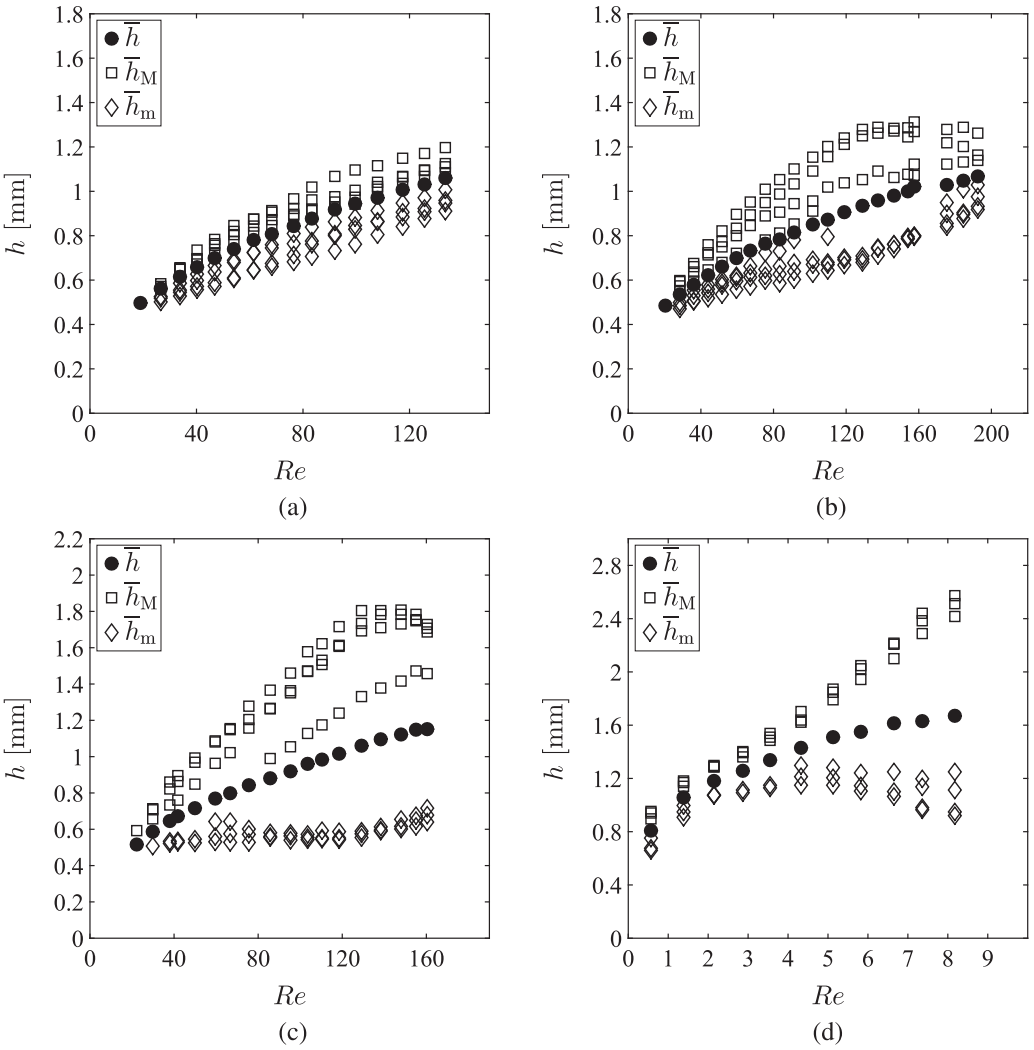

FIG. 18. Mean film heights, $\overline{h}$, rivulet-crest heights, $\overline{h}_{\mathrm{M}}$, and rivulet-trough heights, $\overline{h}_{\mathrm{m}}$, plotted against the flow Re for all examined flow conditions. (a) Ka = 330, $\beta = -15^{\circ}$, (b) Ka = 330, $\beta = -30^{\circ}$, (c) Ka = 330, $\beta = -45^{\circ}$, and (d) Ka = 13.1, $\beta = -30^{\circ}$.

$\sigma_{\mathrm{h,M}}$, and $\sigma_{\mathrm{h,m}}$ are calculated. The rivulet crests and troughs that were identified by application of this procedure to the $\overline{h}_{\mathrm{x}}$ data presented in Fig. 17(a) are shown in Fig. 17(b), along with the local σ_{x} values.

Referring to the data presented in Fig. 18, we observe that $\overline{h}$ increases monotonically with the flow Re, and in accordance with the trend first proposed by Nusselt (see Ref. [66]) and later confirmed by numerous film-flow investigations using different fluids and inclination angles. Owing, however, to the small number of rivulets that are present within the imaged domain, direct comparisons between the $\overline{h}$ values obtained for different Ka and β must be approached with caution. Instead, we focus our analysis on the relative magnitudes of $\overline{h}$, $\overline{h}_{\mathrm{M}}$, and $\overline{h}_{\mathrm{m}}$.

At the smallest negative inclination angle in Fig. 18(a), $\beta = -15^{\circ}$, the disparity among $\overline{h}$, $\overline{h}_{\mathrm{M}}$, and $\overline{h}_{\mathrm{m}}$ is relatively small throughout the examined Re range. In addition, both $\overline{h}_{\mathrm{M}}$ and $\overline{h}_{\mathrm{m}}$ increase monotonically and almost at the same rate with increasing Re. When $\beta = -30^{\circ}$, $\overline{h}_{\mathrm{M}}$ and $\overline{h}_{\mathrm{m}}$ initially

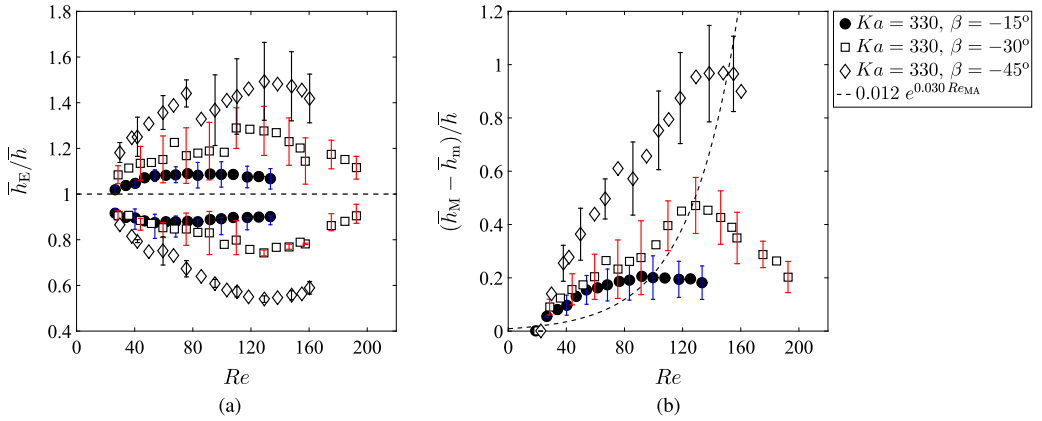

FIG. 19. (a) Averaged (over all detected rivulets) $\overline{h}_M/\overline{h}$ and $\overline{h}_m/\overline{h}$ against Re for all examined flow conditions (Re, β) with Ka = 330. (b) Mean relative rivulet amplitude, $(\overline{h}_M - \overline{h}_m)/\overline{h}$, against Re for Ka = 330.

increase with flow Re; however, $\overline{h}_M$ increases faster than both $\overline{h}_m$ and $\overline{h}$ until Re $\approx$ 130, at which point the rivulet growth is arrested and the crest heights start falling until Re $\approx$ 190. The rivulet troughs, in contrast, display the opposite trend; their heights increase less than either $\overline{h}$ and $\overline{h}_M$ up to Re $\approx$ 130, and then grow faster. When $\beta = -45^\circ$, the same trend with regard to the $\overline{h}_M$ data is observed; the rivulet-trough heights, however, seem to be near-constant at $\overline{h}_m \approx 0.55$ mm until Re $\approx$ 120, at which point the $\overline{h}_m$ starts rising and $\overline{h}_M$ starts falling. In the results relating to the Ka = 13.1 and $\beta = -30^\circ$ flows, we observe that the $\overline{h}_M$ values are more closely clustered than in the previously discussed cases and increase almost linearly with the flow Re, while $\overline{h}_m$ increases until a maximum at Re $\approx$ 5 and then decreases.

In Fig. 19(a), we revisit these results by plotting $\overline{h}_M/\overline{h}$ and $\overline{h}_m/\overline{h}$ (averaged over all rivulets detected in a given flow condition) as a function of Re for all examined film flows with Ka = 330. The normalized extrema, $\overline{h}_E/\overline{h}$, that lie below the line $\overline{h}_E/\overline{h} = 1$ correspond to $\overline{h}_m/\overline{h}$ data, while those that lie above the same line correspond to $\overline{h}_M/\overline{h}$ data. The error bars in this plot represent the standard deviations associated with the calculation of $\overline{h}_M/\overline{h}$ and $\overline{h}_m/\overline{h}$. As expected, all three datasets show a degree of symmetry about the $\overline{h}_E/\overline{h} = 1$ line and display the same trends with increasing Re. Specifically, the mean rivulet-crest height first increases and then decreases relative to the mean film height, while the mean rivulet-trough height first decreases and then increases. When $\beta = -15^\circ$, $\overline{h}_M/\overline{h}$ peaks at $\approx$1.1 and $\overline{h}_m/\overline{h}$ reaches a minimum value of $\approx$0.87, both over the range Re $\approx$ 50–110. When $\beta = -30^\circ$ and $\beta = -45^\circ$, $\overline{h}_M/\overline{h}$ and $\overline{h}_m/\overline{h}$ take maximum values of 1.3 (at Re $\approx$ 120) and 1.5 (at Re $\approx$ 130) and minimum values of 0.75 (at Re $\approx$ 130) and 0.55 (at Re $\approx$ 130). Larger error bars are associated with the majority of the data points that lie above $\overline{h}_E/\overline{h} = 1$, which is indicative of the larger fluctuations at the rivulet crests.

Figure 19(b) shows the mean relative rivulet amplitude, defined as $(\overline{h}_M - \overline{h}_m)/\overline{h}$, against the flow Re. When $\beta = -15^\circ$, the rivulet amplitude peaks at only 0.21 (at $\mathrm{Re_{MA}} \approx 90$); however, it attains much larger values at larger negative inclinations, reaching 0.47 (at $\mathrm{Re_{MA}} \approx 130$) and 0.97 (at $\mathrm{Re_{MA}} \approx 150$) when $\beta = -30^\circ$ and -45°, respectively. In the same plot, we also observe that the rate of increase of the mean relative rivulet amplitude with the flow Re is higher at larger negative inclinations. The relation between $\mathrm{Re_{MA}}$ and $(\overline{h}_M - \overline{h}_m)/\overline{h}$ can be described by the exponential function: $(\overline{h}_M - \overline{h}_m)/\overline{h} = 0.012 \times e^{0.030 \times Re_{MA}}$, with a coefficient of determination $R^2 \approx 0.99$. Close inspection of the $\beta = -15^\circ$ and $\beta = -30^\circ$ data reveals that when the flow Re is increased above $\mathrm{Re_{MA}}$ (i.e., the value at which the rivulet amplitude is maximum), the rivulet amplitude decreases more quickly with the flow Re for $\beta = -30^\circ$ than for $\beta = -15^\circ$.

We now proceed to examine the film-height standard deviation, σ_h, in Fig. 20; equivalent observations can be made by considering the relative standard deviation (normalized with respect

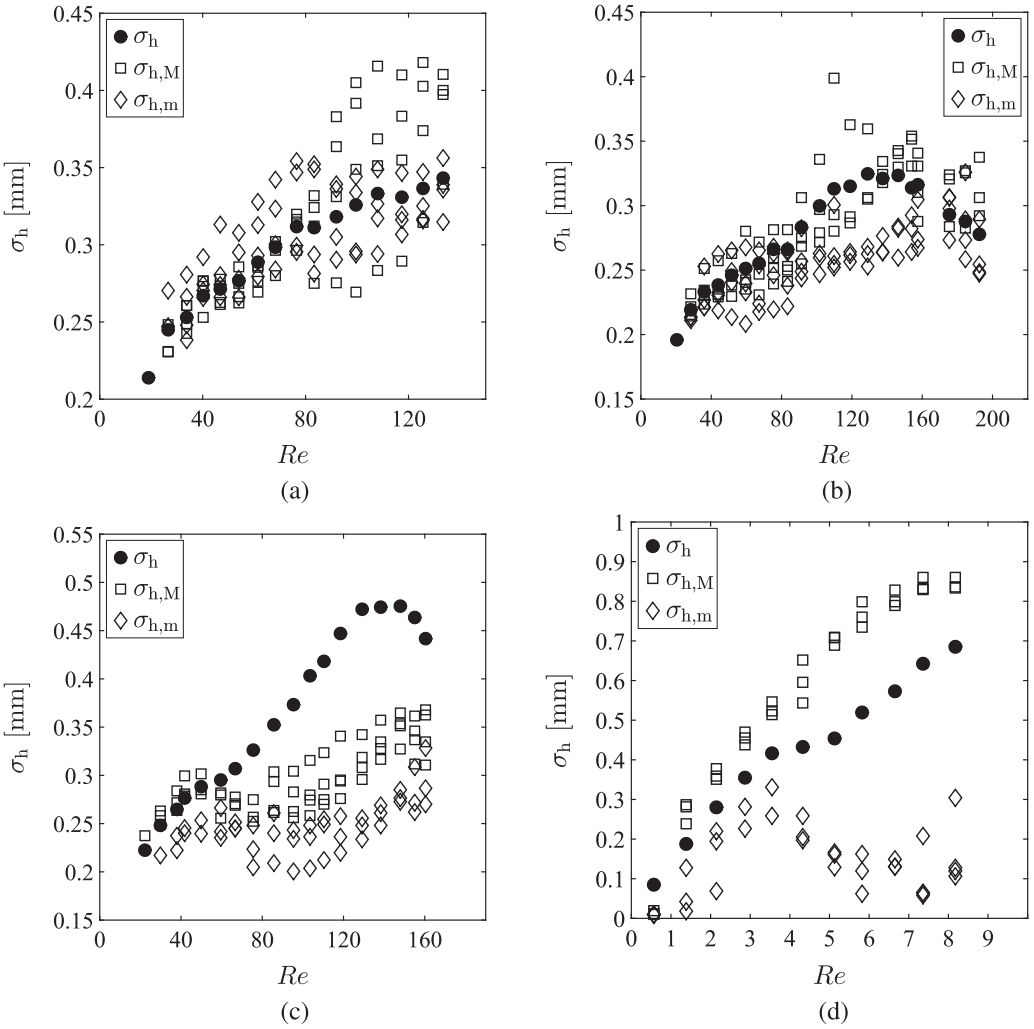

FIG. 20. Film-height standard deviations, σ_h, rivulet-crest height standard deviations, $\sigma_{h,M}$, and rivulet-trough height standard deviations, $\sigma_{h,m}$, plotted against the flow Re for all examined flow conditions. (a) Ka $=$ 330, $\beta = -15^\circ$, (b) Ka $=$ 330, $\beta = -30^\circ$, (c) Ka $=$ 330, $\beta = -45^\circ$, and (d) Ka $=$ 13.1, $\beta = -30^\circ$.

to the corresponding local mean) or the coefficient of variation of the film height, $\sigma_h/\overline{h}$. Despite the significant scatter in the data and with some notable exceptions, it can be seen that σ_h, $\sigma_{h,m}$, and $\sigma_{h,M}$ generally increase with the flow Re; however, as $\overline{h}$, $\overline{h}_M$, and $\overline{h}_m$ increase more by comparison, this leads to lower respective values of film-height coefficient of variation over the examined Re range. Figure 20(a) shows results at the smallest negative inclination-angle. When $\beta = -15^\circ$, we observe that $\sigma_{h,M}$ is typically higher than $\sigma_{h,m}$ below Re $\approx$ 90, and then lower above this value, while σ_h always lies between the two. On the other hand, Fig. 20(b) shows that increasing β to -30° leads to a different behavior. In this plot, the slope of σ_h increases sharply above Re $\approx$ 90, but then stops increasing and reaches a maximum at Re $\approx$ 130, and subsequently decreases at even higher Re. Similar trends are observed for $\beta = -45^\circ$, specifically, the slope of σ_h on these plots increases sharply at Re $\approx$ 60, stops increasing at Re $\approx$ 130, attains a maximum, and subsequently decreases until Re $\approx$ 160. The majority of the $\sigma_{h,M}$ data points lie higher than their $\sigma_{h,m}$ equivalents, while the σ_h data points lie consistently, and above Re $\approx$ 60 also significantly, higher than either.

Close inspection of the variation of σ_h with the flow Re, and the variation of the rivulet amplitude with the flow Re for $\beta = -30^\circ$ and $\beta = -45^\circ$, reveals that the former is dominated by the latter. Moreover, for the same flow Re, the local σ_h (i.e., the σ_h at the rivulet crests and troughs) is lower for the cases with more pronounced rivulet formation. This finding can be interpreted on the basis that the increased azimuthal curvature associated with the former dampens the amplitude of any interfacial waves. Further evidence in support of this "quasistabilizing" effect that rivulets have on the film surface can be found in the $\sigma_h/\overline{h}$ data, which suggest that even though the overall $\sigma_h/\overline{h}$ increases when the rivulet amplitude increases and vice versa, the more pronounced rivulets encountered at high Re when $\beta = -30^\circ$ or -45° suppress the $\sigma_{h,M}/\overline{h}_M$ and $\sigma_{h,m}/\overline{h}_m$ values appreciably.

With reference to the Ka = 13.1 and $\beta = -30^\circ$ results that are presented in Fig. 20(d), we observe that σ_h, $\sigma_{h,M}$, and $\sigma_{h,m}$ are approximately equal to zero at Re = 0.6 (i.e., while the film surface is very smooth and populated by low-amplitude rivulets) and increase as solitary pulses of varying amplitude emerge and grow over the range Re = 0.6–3.5. Above Re = 3.5, any large-amplitude waves migrate to the rivulet crests and the waviness at the troughs starts to fall as evidenced by the reduction in both $\sigma_{h,m}$ and $\sigma_{h,m}/\overline{h}_m$. Meanwhile, $\sigma_{h,M}$ continues to increase at approximately the same rate as the amplitude of the pulses riding the rivulets, as does σ_h, despite the significant drop in $\sigma_{h,m}$. At Re $\approx$ 7, the increase of $\sigma_{h,M}$ stops while $\sigma_{h,m}$ starts to increase again.

C. Wave frequency analysis

Here we consider the occurrence of hydrodynamic waves on the free surface of the examined film flows by employing power spectral density (PSD) analysis to recover the dominant interfacial-wave frequencies on temporally varying film-height data. In more detail, we construct power spectra by applying the fast Fourier transform (FFT) to film-height time series, where each time series constitutes a film-height time record at one location along the imaged flow domain (x) over the entire recording duration (i.e., 10 s), thus comprising 2000 successive data points. Spectra are generated by segmenting each film-height time series into four separate signals, applying a Hamming window to each segment, and averaging the resulting spectra, thus improving the statistical convergence of the spectra, while only modestly affecting our ability to resolve frequency information. Resulting spectra are presented in Fig. 21. When examining the spectral characteristics of flows with Ka = 330, we extracted and later averaged the spectra of time series from 50 locations along the imaging domain, randomly and without replacement. In the case of flows with Ka = 13.1, on the other hand, which exhibited little waviness in the rivulet troughs and a mostly periodic wave behavior in the rivulet crests, we considered data only from the latter.

Unsurprisingly, when $\beta = -15^\circ$ [see Fig. 21(a)], we only observe broadband spectra with no distinct peaks. At Re = 19, the maximum PSD magnitude is found at $f_t = 11.3$ Hz, while with increasing flow Re up to Re $\approx$ 100, the dominant frequency varies in the range $f_t = 8.5$–15.5 Hz [see Fig. 22(b)]. Over the same Re range, the maximum PSD increases only modestly; however, the power at higher frequencies (i.e., when $f \gg f_t$) is enhanced substantially. Increasing the flow Re further, first to Re = 108 and then to Re = 133, has a marked impact on f_t that shifts to 19.7 Hz and then to 22.5 Hz, respectively. The increasing wave frequency with increasing flow Re is already evident in the flow maps presented in Fig. 12. Finally, over the range Re = 83–133, the PSD decreases in the spectral region $f < f_t$ and increases in the region $f > f_t$.

The above description also relates to the results depicted in Fig. 21(b) for flows with $\beta = -30^\circ$. In greater detail, we see that both f_t and PSD(f_t) remain almost unchanged over a large part of the examined Re range (in this case over the range Re $\approx$ 20–150), while the PSD increases for $f \gg f_t$. The dominant frequency increases above $f_t = 15$ Hz at Re $\approx$ 150 and reaches the same level as before (i.e., $f_t = 22.5$) at Re $\approx$ 180. The relation between the wave frequency and the mean flow rate is once again evident in the flow maps of Fig. 7. Similar, though less pronounced, trends are observed in the spectra that were generated when $\beta = -45^\circ$; the dominant frequency increases less than before with the flow Re, peaking at only $f_t = 15.5$ at Re $\approx$ 160, while PSD(f)

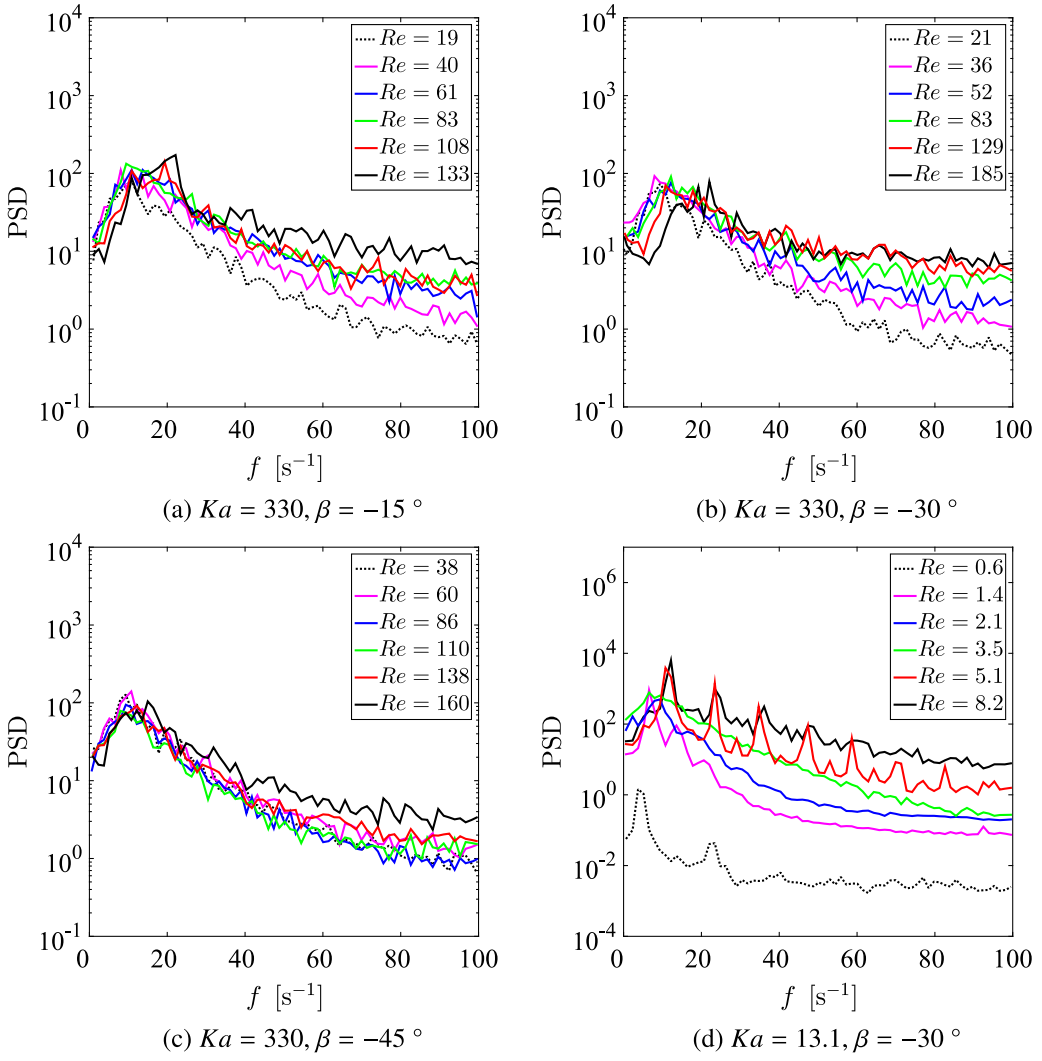

(a) $Ka = 330, \beta = -15\,^\circ$ (b) $Ka = 330, \beta = -30\,^\circ$

(c) $Ka = 330, \beta = -45\,^\circ$ (d) $Ka = 13.1, \beta = -30\,^\circ$

FIG. 21. PSDs for flows with (a) Re = 19–133, Ka = 330, and $\beta = -15^\circ$, (b) Re = 21–185, Ka = 330, and $\beta = -30^\circ$, (c) Re = 30–160, Ka = 330, and $\beta = -45^\circ$, and (d) Re = 0.6–8.2, Ka = 13.1, and $\beta = -30^\circ$.

increases less along the high-frequency regions of the spectra. The observation of higher wave frequencies at smaller negative inclinations and for the same flow Re can be linked to the observation of increased waviness (i.e., higher $\sigma_h/\overline{h}$ values) at the rivulets crests and troughs, and by extension to the less pronounced rivulet formation at smaller negative inclinations and for the same flow Re. Despite contributing an increase in the overall $\sigma_h/\overline{h}$, we also noted earlier that $\sigma_h/\overline{h}$ was lowest at the rivulet crests and troughs for the $\beta = -45^\circ$ flows, followed by the $\beta = -30^\circ$ flows and finally the $\beta = -15^\circ$ for the same flow Re.

Finally, as flows with Ka = 13.1 have been presented elsewhere (see Ref. [11]), we only provide a brief overview of these results here for completeness. At Re = 0.6, the PSD is lowest. As large-amplitude hydrodynamic waves develop on the film surface, the PSD increases by a factor of approximately 10 already from Re = 1.4 and peaks at $f_t = 7.1$ Hz. With increasing Re up to Re = 5.1, the spectra become broadband and gain in power, while the dominant frequency varies in the range $f_t \approx 7$–10 Hz. Then between Re = 5.1 and Re = 8.2, the flow rearranges into

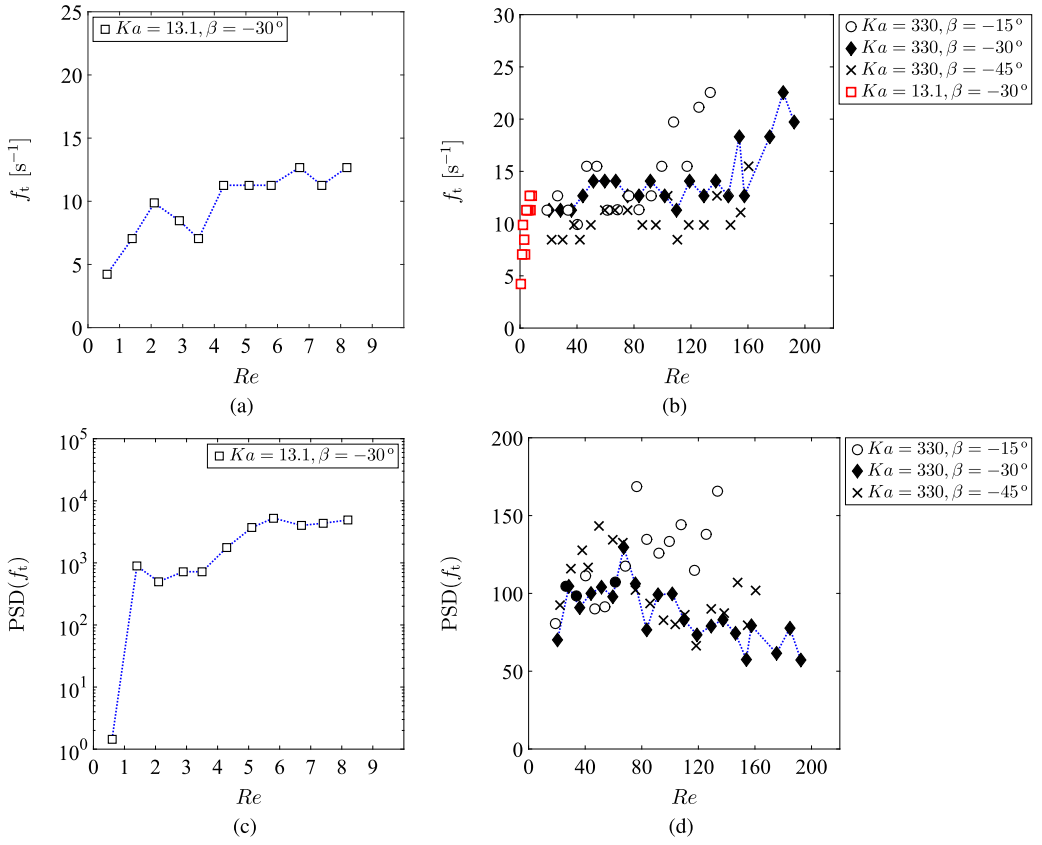

FIG. 22. [(a), (c)] Dominant wave frequencies, f_t, calculated by employment of FFT. [(b), (d)] PSDs, PSD(f_t), corresponding to the peaks in the spectra shown in Fig. 21.

prominent rivulets with large-amplitude drops racing over the crests. The spectra now show distinct, high-density peaks over the range $f_t \approx 11.3$–12.7 Hz while PSD(f_t) continues to increase.

D. Rivulet wavelengths

In this last section, we focus on the rivulet wavelengths across the range of examined flow conditions. These were recovered by first identifying the spanwise coordinates of the rivulet crests and troughs in the time-averaged film-height profiles and then calculating the mean distances between adjacent maxima and minima. Our results are presented separately for each Ka and β combination in Fig. 23, along with the wavelength corresponding to the fastest growing mode for a pendant rivulet, based on the R-T instability mechanism.

As we mentioned in the introduction (Sec. I), the free surface of a thin liquid-film layer suspended underneath a horizontal substrate (i.e., pendant film) deforms according to the R-T instability mechanism [73], with perturbations growing over time and generating a regular pattern of suspended drops [74]. The growth of this instability is determined by the stabilizing action of surface tension and the destabilizing effect of gravity. The distance between adjacent droplets can be calculated from the expression

$$\lambda_{\text{R-T},90^o} = 2\pi\sqrt{2}l_c\,, \tag{5}$$

where $l_c = \sqrt{\sigma/\rho g}$ is the capillary wavelength [53]. When the substrate is tilted, like in our experiments, the substrate inclination affects this instability to the extent that it could disappear

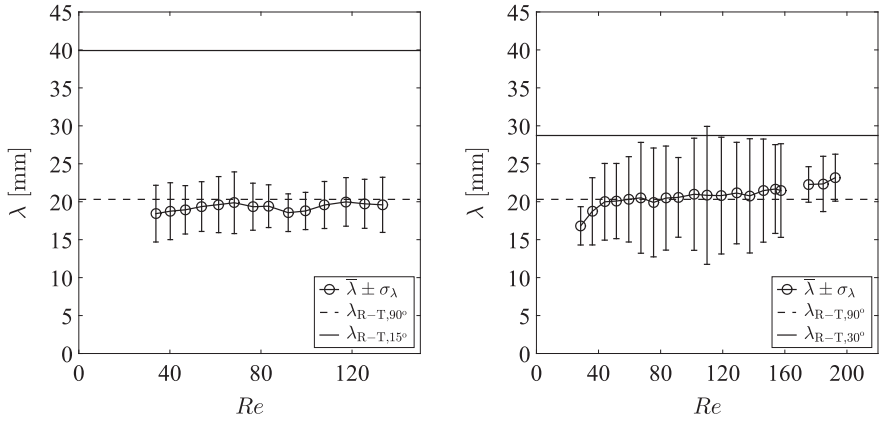

(a) $Ka = 330, \beta = -15\ ^\circ$

(b) $Ka = 330, \beta = -30\ ^\circ$

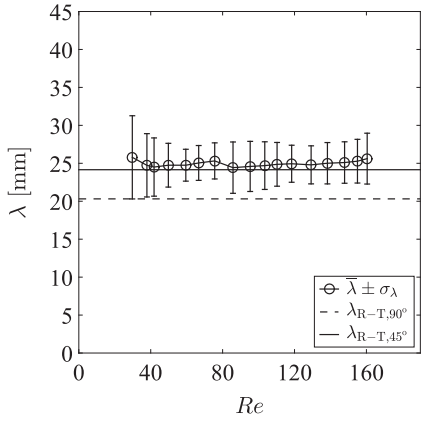

(c) $Ka = 330, \beta = -45\ ^\circ$

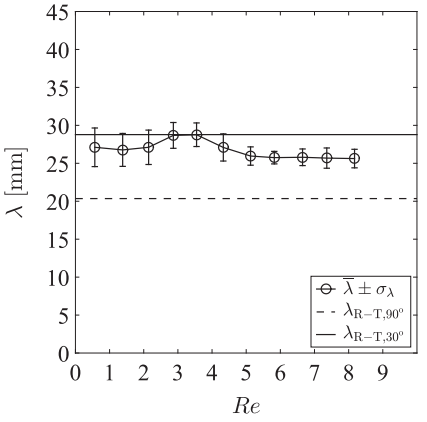

(d) $Ka = 13.1, \beta = -30\ ^\circ$

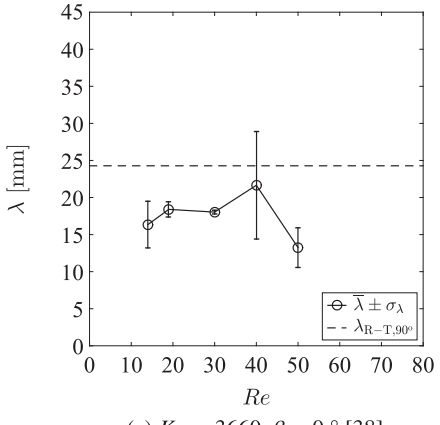

(e) $Ka = 3660, \beta = 0\ ^\circ$ [38]

FIG. 23. Rivulet wavelengths, λ, obtained from the mean distance between adjacent rivulet crests and troughs, for flows with (a) Re = 19–133, Ka = 330, and $\beta = -15^\circ$, (b) Re = 21–185, Ka = 330, and $\beta = -30^\circ$, (c) Re = 30–160, Ka = 330, and $\beta = -45^\circ$, and (d) Re = 0.6–8.2, Ka = 13.1, and $\beta = -30^\circ$. (e) Rivulet wavelength obtained by Kharlamov *et al.* [38] for water films falling down a vertical plane (i.e., with $\beta = 0^\circ$). The error bars indicate the standard deviation in the calculation of λ.

altogether, for example, in the limiting case of a vertical substrate. The wavelength of the most unstable mode for a substrate inclined at an angle β from the vertical (i.e., $\beta = 0^\circ$ for a vertical substrate and $\beta = 90^\circ$ for a horizontal) is given by

$$\lambda_{\text{R-T},\beta} = \frac{2\pi\sqrt{2}l_c}{\sqrt{\sin\beta}}. \tag{6}$$

Consequently, as the substrate inclination approaches the vertical (i.e., $\beta \approx 0^\circ$), the wavelength corresponding to the most amplified mode increases, while when it approaches the horizonal ($\beta = 90^\circ$), the wavelength corresponding to the most amplified mode matches that of the canonical R-T system. For the water-glycerol solutions employed in our experiments, this is ≈20 mm. Prior to commencing with a presentation of our results we would also like to note that according to the analysis by Scheid and coworkers [54], our experimental conditions relate to the convectively unstable flow regime, where convective transport dominates the growth of the R-T instability. In greater detail, the authors plot the critical angle for the absolute-convective instability transition as a function of the flow Re for different Ka. For a fixed Ka, the curve exhibits a minimum corresponding to the smallest negative inclination for which an absolute instability regime can exist, with the region of convective transport to the left of the minimum dominated by surface tension and to the right by inertia. As the liquid Ka is increased, the critical inclination angle shifts toward larger negative inclinations. For the Ka = 13.1 water-glycerol solution we employ, this critical inclination angle corresponds to $\approx -66^\circ$, and to almost -80° for Ka = 330; in our experiments, $\beta \leqslant -45^\circ$, which lies comfortably within the convectively unstable regime.

When $\beta = -30^\circ$ and Ka = 13.1 [Fig. 23(d)], the mean rivulet wavelength increases from $\lambda = 27$ mm at Re = 0.6 to $\lambda = 28.7$ mm in the range Re = 2.8–3.5 (i.e., the range over which we did not identify regular hydrodynamic waves on the film surface), matching remarkably well the wavelength calculated using Eq. (6) with $\beta = 30^\circ$. At even higher Re, the flow reorganizes into sequences of solitary pulses that travel over the rivulets, and the wavelength decreases gradually to $\lambda = 25.6$ mm at Re = 8.2. In Ref. [11], we attributed the nonmonotonic variation of λ with Re to the presence of rivulets and the shrinkage of the film with increasing distance form the flow inlet. In particular, we proposed that the rivulets observed at $x = 330$ mm formed some distance upstream of the PLIF imaging location and as the film contracted, they were "compressed." Thus, over the range Re = 2.8–3.5 where rivulets are not clearly discernible, the observed wavelengths match very closely the most amplified mode of the R-T instability. When Ka = 330 [Figs. 23(a)–23(c)], the observed wavelengths show a weak dependence on the inclination angle. For the smallest negative inclination (i.e., $\beta = -15^\circ$), $\lambda = 18.4$ mm at Re = 34; λ then increases to $\lambda = 19.8$ mm until Re = 68, decreases over the range Re = 68–92 to $\lambda = 18.6$ mm, and finally increases again to $\lambda \approx 20$ mm over the range Re = 117–133. The R-T instability wavelength, when corrected for the inclination angle, is equal to 40 mm; hence, all observed wavelengths fall significantly short of this value and instead match rather closely the R-T instability wavelength for a horizontal substrate. When $\beta = -30^\circ$, $\lambda = 16.8$ mm at Re = 28, then attains $\lambda = 20.3$ mm over the range Re = 51–83, and continues to increase up to $\lambda = 23.2$ mm, again matching closely the R-T instability wavelength for a horizontal substrate over most of the examined Re range. When $\beta = -45^\circ$, however, the observed wavelengths are longer, only vary between $\lambda = 24.5$ and 25.8 mm, and match very closely the wavelength calculated using Eq. (6) with $\beta = 45^\circ$.

In light of these observations and also considering the results of Kharlamov *et al.* [38] for water films falling down a vertical plane [included in Fig. 23(e)], we propose the following mechanism to describe the variation of the observed rivulet wavelengths with the flow Re and the inclination angle β: Given that the rivulet wavelengths that were observed by Kharlamov *et al.* [38] were of the order ≈20 mm, matching closely the wavelength corresponding to the classical R-T instability [see Eq. (5)] irrespective of the imposition of perturbations at the inlet by a regular array of needles, it is reasonable to assume that those rivulets arose from the destabilization of suspended 2-D wavefronts by the R-T instability mechanism. The 2-D wavefronts arise from the primary hydrodynamic

instability, while their spanwise modulations arise from a secondary instability. Further evidence of the destabilization of a liquid hump or ridge (like the ridge that produces the "tears of wine") by the R-T instability can be found in numerous studies; see, for example, Refs. [60,62,75]. We conjecture that in our study, this mechanism may account for the results in Figs. 23(a) and 23(b), where the mean rivulet wavelengths match closely the R-T wavelength irrespective of the flow Re. When the substrate (negative) inclination is increased further [see, for example, Fig. 23(c)], the observed wavelengths match closely the ones that arise from the destabilization of a flat-film coating the underside of an inclined plate by the *primary* R-T instability (see Eq. (6) and Ref. [53]). Thus, with increasing negative inclination from the vertical, the contribution of the R-T mechanism is augmented over all other mechanisms that destabilize the flow, such as the Rayleigh-Plateau mechanism or inertia (see, for example, Ref. [26]). This transition will be analyzed in greater detail in a future study.

As a final remark, we would like to note that the mode selection should not depend on the downstream location where the PLIF data are collected, as it appears to be almost independent of the flow Re, which changes proportionally to the film contraction. Nevertheless, the lateral compression experienced by the film will promote the merging of adjacent rivulets which will, in turn, manifest in an increase of the observed rivulet wavelengths. This phenomenon was reported, for example, by Zhang and coworkers in their study of the of the interface topology and shrinkage behavior of heated water films [49] and is also characteristic of films flowing down the underside of inclined substrates [46,50]. Given that the downstream distance where we carry out our PLIF measurements is relatively short and that the shrinkage of the examined films is weak, the merging of adjacent rivulets upstream of the measurement location is highly unlikely. Furthermore, the span of our test section is large enough to accommodate in excess of 10 rivulets, and hence any merging should only have a limited effect on our rivulet wavelength measurements. Nevertheless, it is imperative for future experimental investigations to include measurements of flow development along the streamwise direction, as well as comparisons between experimentally recovered rivulet wavelengths and values predicted by appropriate numerical models, which could offer a deeper theoretical understanding of the flow phenomena underlying these flows.

VII. CONCLUSIONS

A measurement technique based on PLIF was employed to recover space- and time-resolved film-height measurement data in thin liquid films flowing under an inclined planar substrate. Our experimental campaign comprised four measurement sets and spanned different flow rates, inclination angles, and liquid viscosities, covering the following range of conditions: (i) for $\beta = -15^\circ$ and Ka = 330, Re = 19–133, (ii) for $\beta = -30^\circ$ and Ka = 330, Re = 21–193, (iii) for $\beta = -45^\circ$ and Ka = 330, Re = 22–160, and finally (iv) for $\beta = -30^\circ$ and Ka = 13.1, Re = 0.6–8.2, where β is defined as negative with respect to the vertical. The collection optics were arranged to image a flow region extending ≈40 mm symmetrically on either side of the middle of the film span, at a distance of 330 mm downstream of the flow inlet. Additional measurements were conducted near the film rim, with the collection optics arranged to visualize a section of the flow extending ≈40 mm from the film contact line.

Depending on the imposed flow conditions, a range of flow regimes were identified, typically characterized by strong three-dimensionality and pronounced rivulet formation. For the lower Ka (=13.1) liquid and the intermediate β ($= -30^\circ$), we observed smooth films populated by rivulets at Re = 0.6, a complex interface in the range Re = 1.5–3.4, and regular sequences of solitary pulses traveling over the rivulets at higher Re (see also Ref. [6]). For the higher Ka (=330) liquid, the film surface was populated by U- and W-shaped solitary pulses below Re ≈ 30, whereas in the range Re ≈ 30–50, the development of smaller and faster pulses triggered the formation of rivulets. The amplitude of these rivulets increased with the flow Re, until Re ≈ 130. Quasi-2-D wavefronts that extended along the entire imaged domain and protruded marginally at the rivulet crests were also observed intermittently and became more frequent at higher Re, resulting in

appreciable mass transport across the rivulet troughs. Thus, with increasing inertia, more liquid was directed into the rivulet troughs, reducing the rivulet amplitude above Re $\approx$ 130. A similar topology was observed at the largest negative inclination of $\beta = -45^\circ$, but with larger amplitude rivulets. At the smallest negative inclination of $\beta = -15^\circ$, the film-height modulation along the transverse direction of the flow was relatively weak, while above Re $\approx$ 80, the wide quasi-2-D waves were the dominant interfacial feature. Adjacent to the film contact line, the flow was bounded by a rivulet which was higher than any of the rivulets that were observed in the middle of the film span. The height of this feature was found to increase with the flow Re for all examined β.

Postprocessing methodologies were applied to the film-height data in order to characterize the interface topology. The PDFs that were generated for flows with Ka = 330 displayed more symmetric shapes and a pronounced "swelling" (skewness) to the right of the main peaks at higher flow Re. This effect was amplified at the largest negative inclination ($\beta = -45^\circ$). The mean film height, $\overline{h}$, increased monotonically with the flow Re, and in accordance with the trend first proposed by Nusselt, over all examined flow conditions. For the smallest negative inclination angle ($\beta = -15^\circ$), both the mean height of the rivulet crests, $\overline{h}_{\mathrm{M}}$, and the mean height of the rivulet troughs, $\overline{h}_{\mathrm{m}}$, increased monotonically with the flow Re. However, at the intermediate inclination angle ($\beta = -30^\circ$), $\overline{h}_{\mathrm{M}}$ increased more than $\overline{h}_{\mathrm{m}}$ and $\overline{h}$ with increasing Re, until Re $\approx$ 130; it then saturated and decreased at even higher Re. When $\beta = -45^\circ$, $\overline{h}_{\mathrm{M}}$ peaked at Re $\approx$ 120, while $\overline{h}_{\mathrm{m}}$ only started increasing above Re $\approx$ 120. As a result, the mean amplitude of the rivulets attained larger values at larger negative inclinations, peaking at 0.21 (at $\mathrm{Re}_{\mathrm{MA}} \approx 90$) when $\beta = -15^\circ$, 0.47 (at $\mathrm{Re}_{\mathrm{MA}} \approx 130$) when $\beta = -30^\circ$, and 0.97 (at $\mathrm{Re}_{\mathrm{MA}} \approx 150$) when $\beta = -45^\circ$.

The film waviness was examined based on the "global" film-height standard deviation, σ_{h}, and the local film-height standard deviations, $\sigma_{\mathrm{h,M}}$ and $\sigma_{\mathrm{h,m}}$, at the rivulet crests and troughs. For flows with Ka = 330 and $\beta = -15^\circ$, σ_{h}, $\sigma_{\mathrm{h,m}}$, and $\sigma_{\mathrm{h,M}}$ increased over the examined range of Re, whereas for flows with $\beta = -30^\circ$, σ_{h} increased until Re $\approx$ 130 and decreased thereafter. The same (nonmonotonic) behavior was observed when $\beta = -45^\circ$, with σ_{h} increasing until Re $\approx$ 130 and decreasing thereafter. For the same inclination angle, $\sigma_{\mathrm{h,M}}$ was typically larger than $\sigma_{\mathrm{h,m}}$, while σ_{h} was consistently larger than both and significantly so above Re $\approx$ 60. This behavior was less pronounced when $\beta = -30^\circ$, with σ_{h} attaining higher values than $\sigma_{\mathrm{h,m}}$ but not $\sigma_{\mathrm{h,M}}$ for Re > 80, and was not observed at all when $\beta = -15^\circ$. The variation of these statistical quantities was linked to the variation of the rivulet amplitudes with the flow Re and β. Specifically, for the same flow Re, the σ_{h} values recovered from the rivulet crests and troughs are lower for the cases with more pronounced rivulet formation (i.e., at higher negative inclinations). This "quasistabilizing" effect that the rivulets induce can be understood on the basis that the increased azimuthal curvature associated with the former dampens any interfacial waves.

Finally, we analyzed the occurrence of hydrodynamic waves on the film surface by performing a PSD analysis on temporally varying film-height data. For Ka = 330, we only observed broadband spectra with no strong district peaks. At the smallest negative inclination angle of $\beta = -15^\circ$, the dominant frequency varied in the range $f_{\mathrm{t}} = 8.5$–15.5 Hz below Re $\approx$ 100, and then increased to 22.5 Hz at Re = 133. Over the same Re range, the power over the high-frequency regions of the spectra (i.e., at $f \gg f_{\mathrm{t}}$ Hz) increased substantially. At $\beta = -30^\circ$ and $\beta = -45^\circ$, $f_{\mathrm{t}} = 22.5$ Hz at Re $\approx$ 180 and $f_{\mathrm{t}} = 15.5$ Hz at Re $\approx$ 160, respectively. The observation of higher wave frequencies at smaller negative inclinations for the same flow Re was linked to the observation of increased waviness (i.e., higher σ_{h} values) at the rivulets crests and troughs, and by extension to the less pronounced rivulet formation. For Ka = 13.1 instead, we observed quasiperiodic flows at Re = 1.4, as well as over the range Re = 5.1–8.2, with distinct high-density peaks at $f_{\mathrm{t}} = 7.1$ Hz in the first instance, and over the range $f_{\mathrm{t}} \approx 11.3$–$12.7$ Hz in the latter. For the same flows, the mean rivulet wavelength first increased to $\lambda = 28.7$ mm over the range Re = 2.8–3.5, matching the wavelength of the fastest growing mode for a pendant rivulet based on the R-T instability mechanism (accounting for the inclination angle), and then decreased to $\lambda = 25.6$ mm at Re = 8.2. When Ka = 330 and for the same flow Re, the mean rivulet wavelength increased with increasing negative inclination angle and matched the value calculated based on the R-T instability with $\beta = -45^\circ$.

Based on these results, we hypothesize that the rivulet wavelengths observed when $\beta = -15^\circ$ or -30° (for Ka = 330) arise from the destabilization of suspended 2-D wavefronts by a secondary R-T instability mechanism that would be of interest to explore further. On the other hand, for larger negative inclinations, the observed wavelengths match closely those arising from the destabilization of a flat-film coating the underside of an inclined plate by the primary R-T instability mechanism.

ACKNOWLEDGMENTS

This work was supported by the UK Engineering and Physical Sciences Research Council (EPSRC) [Grants No. EP/K008595/1, No. EP/L020564/1, and No. EP/M021556/1]. Benoit Scheid would also like to thank the BELSPO Agency [Grant No. IAP-7/38 MicroMAST] and the F.R.S.–FNRS for financial support.

Data supporting this publication can be obtained on request from cep-lab@imperial.ac.uk.

[1] P. L. Kapitza, Wave flow of thin layers of a viscous fluid: I. Free flow, J. Exp. Theor. Phys. **18**, 3 (1948).

[2] P. L. Kapitza and S. P. Kapitza, Wave flow of thin layers of a viscous fluid: III. Experimental study of undulatory flow conditions, J. Exp. Theor. Phys. **19**, 105 (1949).

[3] A. Charogiannis, J. S. An, and C. N. Markides, A simultaneous planar laser-induced fluorescence, particle image velocimetry, and particle tracking velocimetry technique for the investigation of thin liquid-film flows, Exp. Therm. Fluid Sci. **68**, 516 (2015).

[4] A. Charogiannis, F. Denner, B. G. M. van Wachem, S. Kalliadasis, and C. N. Markides, Detailed hydrodynamic characterization of harmonically excited falling-film flows: A combined experimental and computational study, Phys. Rev. Fluids **2**, 014002 (2017).

[5] F. Denner, A. Charogiannis, M. Pradas, C. N. Markides, B. G. M. van Wachem, and S. Kalliadasis, Solitary waves on falling liquid films in the inertia-dominated regime, J. Fluid Mech. **837**, 491 (2018).

[6] A. Charogiannis, F. Denner, B. G. M. van Wachem, S. Kalliadasis, and C. N. Markides, Statistical characteristics of falling-film flows: A synergistic approach at the crossroads of direct numerical simulations and experiments, Phys. Rev. Fluids **2**, 124002 (2017).

[7] A. Cherdantsev, D. B. Hann, and B. J. Azzopardi, Study of gas-sheared liquid film in horizontal rectangular duct using high-speed LIF technique: Three-dimensional wavy structure and its relation to liquid entrainment, Int. J. Multiphase Flow **67**, 52 (2014).

[8] I. Zadrazil, O. K. Matar, and C. N. Markides, An experimental characterization of downwards gas-liquid annular flow by laser-induced fluorescence: Flow regimes and film statistics, Int. J. Multiphase Flow **60**, 87 (2014).

[9] I. Zadrazil and C. N. Markides, An experimental characterization of liquid films in downwards co-current gas-liquid annular flow by particle image and tracking velocimetry, Int. J. Multiphase Flow **67**, 42 (2014).

[10] G. Karimi and M. Kawaji, Flow characteristics and circulatory motion in wavy falling films with and without counter-current gas flow, Int. J. Multiphase Flow **25**, 1305 (1999).

[11] A. Charogiannis and C. N. Markides, Application of planar laser-induced fluorescence for the investigation of interfacial waves in liquid-films flowing under inverted substrates, Interfacial Phenom. Heat Transf. **4**, 235 (2016).

[12] C. S. Yih, Stability of liquid flow down an inclined plane, Phys. Fluids **6**, 321 (1963).

[13] E. J. Hinch, A note on the mechanism of the instability at the interface between two shearing fluids, J. Fluid Mech. **144**, 463 (1984).

[14] R. E. Kelly, D. A. Goussis, S. P. Lin, and F. K. Hsu, The mechanism for surface wave instability in film flow down an inclined plane, Phys. Fluids **1**, 819 (1989).

[15] M. K. Smith, The mechanism for the long-wave instability in thin liquid films, J. Fluid Mech. **217**, 469 (1990).

[16] S. Kalliadasis, C. Ruyer-Quil, B. Scheid, and M. G. Velarde, *Falling Liquid Films*, Applied Mathematical Sciences Vol. 176 (Springer Verlag, Berlin, 2012).

[17] J. Liu, J. D. Paul, and J. P. Gollub, Measurements of the primary instabilities of film flows, J. Fluid Mech. **250**, 69 (1993).
[18] J. Liu and J. P. Gollub, Onset of Spatially Chaotic Waves on Flowing Films, Phys. Rev. Lett. **70**, 2289 (1993).
[19] J. Liu and J. P. Gollub, Solitary wave dynamics of film flows, Phys. Fluids **6**, 1702 (1994).
[20] J. Liu, J. B. Schneder, and J. P. Gollub, Three-dimensional instabilities of film flows, Phys. Fluids **7**, 55 (1995).
[21] T. Nosoko, P. N. Yoshimura, T. Nagata, and K. Oyakawa, Characteristics of two-dimensional waves on falling liquid films, Chem. Eng. Sci. **51**, 725 (1996).
[22] T. Nosoko and A. Miyara, The evolution and subsequent dynamics of waves on a vertically falling liquid film, Phys. Fluids **16**, 1118 (2004).
[23] B. Ramaswamy, S. Chippada, and S. W. Joo, A full-scale numerical study of interfacial instabilities in thin-film flows, J. Fluid Mech. **325**, 163 (1996).
[24] K. Argyriadi, K. Serifi, and V. Bontozoglou, Nonlinear dynamics of inclined films under low-frequency forcing, Phys. Fluids **16**, 2457 (2004).
[25] B. Scheid, C. Ruyer-Quil, and P. Manneville, Wave patterns in film flows: Modelling and three-dimensional waves, J. Fluid Mech. **562**, 183 (2006).
[26] N. Kofman, S. Mergui, and C. Ruyer-Quil, Three-dimensional instabilities of quasi-solitary waves in falling liquid films, J. Fluid Mech. **757**, 854 (2014).
[27] M. Rietz, R. Rohlfs, W. adn Kneer, and B. Scheid, Experimental investigation of thermal structures in regular three-dimensional falling films, Eur. Phys. J.-Spec. Top. **224**, 355 (2015).
[28] S. V. Alekseenko, V. A. Antipin, V. V. Guzanov, S. M. Kharlamov, and D. M. Markovich, Three-dimensional solitary waves on falling liquid film at low Reynolds numbers, Phys. Fluids **17**, 121704 (2005).
[29] E. A. Demekhin, E. N. Kalaidin, S. Kalliadasis, and S. Yu. Vlaskin, Three-dimensional localized coherent structures of surface turbulence. I. Scenarios of two-dimensional–three-dimensional transition, Phys. Fluids **19**, 114103 (2007).
[30] E. A. Demekhin, E. N. Kalaidin, S. Kalliadasis, and S. Y. Vlaskin, Three-dimensional localized coherent structures of surface turbulence. II. Λ solitons, Phys. Fluids **19**, 114104 (2007).
[31] E. A. Demekhin, E. N. Kalaidin, and A. S. Selin, Three-dimensional localized coherent structures of surface turbulence. III. Experiment and model validation, Phys. Fluids **22**, 092103 (2010).
[32] E. A. Demekhin, E. N. Kalaidin, S. Kalliadasis, and S. Y. Vlaskin, Three-dimensional localized coherent structures of surface turbulence: Model validation with experiments and further computations, Phys. Rev. E **82**, 036322 (2010).
[33] P. N. Yoshimura, T. Nosoko, and T. Nagata, Enhancement of mass transfer into a falling laminar liquid film by two-dimensional surface waves: Some experimental observations and modelling, Chem. Eng. Sci. **51**, 1231 (1996).
[34] C. D. Park and T. Nosoko, Three-dimensional wave dynamics on a falling film and associated mass transfer, AIChE **49**, 2715 (2003).
[35] P. Adomeit and U. Renz, Hydrodynamics of three-dimensional waves in laminar falling films, Int. J. Multiphase Flow **26**, 1183 (2000).
[36] S. V. Alekseenko, V. V. Guzanov, D. M. Markovich, and S. M. Kharlamov, Specific features of a transition from the regular two-dimensional to three-dimensional waves on falling liquid films, Tech. Phys. Lett. **38**, 739 (2012).
[37] S. V. Alekseenko, A. V. Bobylev, V. V. Guzanov, D. M. Markovich, and S. M. Kharlamov, Formation of rivulets in isothermal liquid film flow during transition to a three-dimensional wave regime, Tech. Phys. Lett. **40**, 1031 (2014).
[38] S. M. Kharlamov, V. V. Guzanov, A. V. Bobylev, S. V. Alekseenko, and D. M. Markovich, The transition from two-dimensional to three-dimensional waves in falling liquid films: Wave patterns and transverse redistribution of local flow rates, Phys. Fluids **27**, 114106 (2015).

[39] E. A. Chinnov and O. A. Kabov, Marangoni effect on wave structure in liquid films, Microgravity Sci. Technol. **19**, 18 (2007).
[40] V. V. Lel, A. Kellerman, G. Dietze, R. Kneer, and A. N. Pavlenko, Investigations of the Marangoni effect on the regular structures in heated wavy liquid films, Exp. Fluids **44**, 341 (2008).
[41] E. A. Chinnov and S. S. Abdurakipov, Thermal entry length in falling liquid films at high Reynolds numbers, Int. J. Heat Mass Transfer **56**, 775 (2013).
[42] C. N. Markides, R. Mathie, and A. Charogiannis, An experimental characterization of spatiotemporally resolved heat transfer in thin liquid-film flows falling over an inclined heated foil, Int. J. Heat Mass Transfer **93**, 872 (2016).
[43] S. W. Joo, S. H. Davis, and S. G. Bankoff, A mechanism for rivulet formation in heated falling films, J. Fluid Mech. **321**, 279 (1996).
[44] B. Scheid, S. Kalliadasis, C. Ruyer-Quil, and P. Colinet, Spontaneous channeling of solitary pulses in heated-film flows, Europhys. Lett. **84**, 64002 (2008).
[45] B. Scheid, S. Kalliadasis, C. Ruyer-Quil, and P. Colinet, Interaction of three-dimensional hydrodynamic and thermocapillary instabilities in film flows, Phys. Rev. E **78**, 066311 (2008).
[46] D. A. Rothrock, Study of flows down the underside of an inclined plane, Ph.D. thesis, University of Cambridge, Cambridge, UK, 1968 (unpublished).
[47] F. Zhang, Z. Zhang, and J. Geng, Study on shrinkage characteristics of heated falling films, AIChE **51**, 2899 (2005).
[48] F. Zhang, X. Zhao, J. Geng, Y.-T. Wu, and Z. Zhang, A new insight into Marangoni effect in non-isothermal falling liquid films, Exp. Therm Fluid Sci. **31**, 361 (2007).
[49] F. Zhang, J. Peng, J. Geng, Z.-X. Wang, and Z.-B. Zhang, Thermal imaging study on the surface wave of heated falling liquid films, Exp. Therm Fluid Sci. **33**, 424 (2009).
[50] A. Indeikina, I. Veretennikov, and H.-C. Chang, Drop fall-off from pendant rivulets, J. Fluid Mech. **338**, 173 (1997).
[51] S. V. Alekseenko and S. I. Markovich, D. M. Shtork, Wave flow of rivulets on the outer surface of an inclined cylinder, Phys. Fluids **8**, 3288 (1996).
[52] S. V. Alekseenko, V. A. Antipin, A. V. Bobylev, and D. M. Markovich, Application of PIV to velocity measurements in a liquid film flowing down an inclined cylinder, Exp. Fluids **43**, 197 (2007).
[53] P.-T. Brun, A. Damiano, P. Rieu, G. Balestra, and F. Gallaire, Rayleigh-Taylor instability under an inclined plane, Phys. Fluids **27**, 084107 (2015).
[54] B. Scheid, N. Kofman, and W. Rohlfs, Critical inclination for absolute/convective instability transition in inverted falling films, Phys. Fluids **28**, 044107 (2016).
[55] N. Kofman, W. Rohlfs, F. Gallaire, B. Scheid, and C. Ruyer-Quil, Prediction of two-dimensional dripping onset of a liquid film under inclined plane, Int. J. Multiphase Flow **104**, 286 (2018).
[56] W. Rohlfs, P. Pischke, and B. Scheid, Hydrodynamic waves in films flowing under an inclined plane, Phys. Rev. Fluids **2**, 044003 (2017).
[57] W. Rohlfs and B. Scheid, Phase diagram for the onset of circulating waves and flow reversal in inclined falling films, J. Fluid Mech. **763**, 322 (2015).
[58] T.-S. Lin and L. Kondic, Thin films flowing down inverted substrates: Two dimensional flow, Phys. Fluids **22**, 052105 (2010).
[59] T.-S. Lin, L. Kondic, and A. Filippov, Thin films flowing down inverted substrates: Three dimensional flow, Phys. Fluids **24**, 022105 (2012).
[60] H. E. Huppert, Flow and instability of a viscous current down a slope, Nature (London) **300**, 427 (1982).
[61] S. M. Troian, E. Herbolzheimer, S. A. Safran, and J. F. Joanny, Fingering instabilities of driven spreading films, Europhys. Lett. **10**, 25 (1989).
[62] M. A. Spaid and G. M. Homsy, Stability of Newtonian and viscoelastic dynamic contact lines, Phys. Fluids **8**, 460 (1996).
[63] S. Kalliadasis, Nonlinear instability of a contact line driven by gravity, J. Fluid Mech. **413**, 355 (2000).
[64] M. Rietz, B. Scheid, F. Gallaire, N. Kofman, R. Kneer, and W. Rohlfs, Dynamics of falling films on the outside of a vertical rotating cylinder: Waves, rivulets and dripping transitions, J. Fluid Mech. **832**, 189 (2017).

[65] R. Mathie, H. Nakamura, and C. N Markides, Heat transfer augmentation in unsteady conjugate thermal systems, part II: Applications, Int. J. Heat Mass Transfer **56**, 819 (2013).
[66] W. Nusselt, Die Oberflächenkondensation des wasserdampfes, Zetrschr. Ver. Deutch. Ing. **60**, 541 (1916).
[67] M. Pradas, D. Tseluiko, and S. Kalliadasis, Rigorous coherent-structure theory for falling liquid films: Viscous dispersion effects on bound-state formation and self-organization, Phys. Fluids **23**, 044104 (2011).
[68] G. Balestra, N. Kofman, P.-T. Brun, B. Scheid, and F. Gallaire, Three-dimensional Rayleigh-Taylor instability under a unidirectional curved substrate, J. Fluid Mech. **837**, 19 (2018).
[69] A. Georgantaki, J. Vatteville, M. Vlachogiannis, and V. Bontozoglou, Measurements of liquid film flow as a function of fluid properties and channel width: Evidence for surface-tension-induced long-range transverse coherence, Phys. Rev. E **84**, 026325 (2011).
[70] V. Pollak, A. Haas, and N. Aksel, Side wall effects on the instability of thin gravity-driven films: From long-wave to short-wave instability, Phys. Fluids **23**, 094110 (2011).
[71] T. D. Karapantsios, S. V. Paras, and A. J. Karabelas, Statistical characteristics of free falling films at high Reynolds numbers, Int. J. Multiphase Flow **15**, 1 (1989).
[72] K. Moran, J. Inumaru, and M. Kawaji, Instantaneous hydrodynamics of a laminar wavy liquid film, Int. J. Multiph. Flow **28**, 731 (2002).
[73] D. H. Sharp, An overview of Rayleigh-Taylor instability, Phys. D. (Amsterdam, Neth.) **12**, 3 (1984).
[74] M. Fermigier, L. Limat, J. E. Wesfreid, P. Boudinet, and C. Quilliet, Two-dimensional patterns in Rayleigh-Taylor instability of a thin layer, J. Fluid Mech. **236**, 349 (1992).
[75] J. R. Lister, R. C. Kerr, N. J. Russell, and A. Crosby, Rayleigh-Taylor instability of an inclined buoyant viscous cylinder, J. Fluid Mech. **671**, 313 (2011).